JGR Oceans

RESEARCH ARTICLE
10.1029/2022JC018604

Key Points:

- El Niño anomalies propagating with coastally trapped waves (CTWs) impact the coastal ocean variability off Oregon 2014–2016
- In summers 2014 and 2015, the subsurface along-slope velocity anomalies are poleward, propagating as CTW
- On the shelf, alongshore southward currents are sharply reduced in July 2014 and 2015 despite the upwelling winds are strong

Correspondence to:

A. L. Kurapov,
Alexander.Kurapov@noaa.gov

Citation:

Kurapov, A. L., Rudnick, D. L., Cervantes, B. T., & Risien, C. M. (2022). Slope and shelf flow anomalies off Oregon influenced by the El Niño remote oceanic mechanism in 2014–2016. *Journal of Geophysical Research: Oceans*, *127*, e2022JC018604. https://doi.org/10.1029/2022JC018604

Received 1 MAR 2022
Accepted 17 OCT 2022

Author Contributions:

Conceptualization: Alexander L. Kurapov
Data curation: Daniel L. Rudnick, Brandy T. Cervantes, Craig M. Risien
Formal analysis: Alexander L. Kurapov, Daniel L. Rudnick, Brandy T. Cervantes, Craig M. Risien
Investigation: Alexander L. Kurapov
Methodology: Alexander L. Kurapov, Daniel L. Rudnick, Brandy T. Cervantes, Craig M. Risien
Resources: Daniel L. Rudnick, Brandy T. Cervantes, Craig M. Risien
Validation: Alexander L. Kurapov, Daniel L. Rudnick, Brandy T. Cervantes, Craig M. Risien
Writing – original draft: Alexander L. Kurapov
Writing – review & editing: Alexander L. Kurapov, Daniel L. Rudnick, Brandy T. Cervantes, Craig M. Risien

© 2022. American Geophysical Union. All Rights Reserved. This article has been contributed to by U.S. Government employees and their work is in the public domain in the USA.

Slope and Shelf Flow Anomalies Off Oregon Influenced by the El Niño Remote Oceanic Mechanism in 2014–2016

Alexander L. Kurapov[1], Daniel L. Rudnick[2], Brandy T. Cervantes[3], and Craig M. Risien[3]

[1]National Oceanic and Atmospheric Administration, Coast Survey Development Laboratory, Coastal Marine Modeling Branch (NOAA CSDL/CMMB), Silver Spring, MD, USA, [2]Scripps Institution of Oceanography, La Jolla, CA, USA, [3]College of Earth, Ocean, and Atmospheric Sciences, Oregon State University, Corvallis, OR, USA

Abstract Outputs of the regional ocean circulation model are analyzed to demonstrate the measurable impact of the El Niño remote oceanic forcing mechanism along the US West Coast during the major heat wave period of 2014–2016. The 2-km horizontal resolution model, based on the Regional Ocean Modeling System (ROMS), was run for the period of 2009–2018. Though the model does not assimilate observations, it performs well by comparison with time series data explaining observed variability on temporal scales from several days to seasonal and interannual. The El Niño-related oceanic anomalies provided by a global state estimate are introduced in the regional model at the southern boundary at 24N. These propagate alongshore with coastally trapped waves (CTWs) and influence the variability off Oregon (41°–46°N). In particular, CTWs are evident in the subsurface along-slope current, v_s, and in the depth of the 26.5 kg m^{-3} isopycnal surface over the slope, $z_{26.5}$. In summer 2014 and 2015, v_s anomalies are positive (northward) and $z_{26.5}$ anomalies are negative (deeper) along the US West Coast. In addition to the CTW patterns, $z_{26.5}$ anomalies also exhibit slow-moving features associated with undercurrent widening, separation, and subsurface eddy variability. Over the Oregon shelf, El Niño conditions contributed to the sharp weakening of the southward alongshore current throughout the water column in July 2014 and 2015, despite the near-average southward, upwelling-favorable winds.

Plain Language Summary El Niño is a large-scale anomalous pattern that originates in the atmosphere and the ocean in the equatorial Pacific ocean. It occurs once every several years at irregular time intervals and impacts the weather and ocean variability at great distances, in particular reaching the Pacific coast of the United States. In this study, a high-resolution, three-dimensional computer ocean circulation model is utilized to track the El Niño-related signal propagating as very long oceanic waves along the continental slope from Mexico to the United States and Canada in 2014 and 2015. This propagation is best seen in the subsurface alongshore currents and in the depression of the surfaces of constant density over the continental slope. The model compares well to satellite and in-situ observations. Carefully designed numerical models can be utilized for multiyear simulations to aid scientific discoveries.

1. Introduction

Years 2014–2016 saw one of the most intense and prolonged heat waves along the North-Eastern Pacific (NEP) coast, from the equatorial region to Alaska (Peterson et al., 2017; Jacox et al., 2019). Along the US West Coast, where summer wind-driven upwelling supports high biological productivity (Chavez & Messié, 2009), the heat wave led to serious impacts on the biological composition, diversity, and survival rates at all trophic levels (Cavole et al., 2016; McCabe & Coauthors, 2016; Peterson et al., 2017; Piatt et al., 2020; Suryan et al., 2021). Two large-scale drivers contributed to the heat wave onset in 2014, the "warm blob" and El Niño. The warm blob was the near-surface temperature anomaly formed in the Gulf of Alaska late in 2013 driven by anomalously low winds over the region, resulting in anomalously low cooling by the sensible and latent atmospheric heat fluxes (Amaya et al., 2016; Bond et al., 2015). El Niño was detected in the eastern equatorial region both in satellite and in-situ observations in late 2013 and early 2014 (Jacox et al., 2019; Rudnick et al., 2021). It was halted in mid-2014 by the intensified westerlies but reemerged in 2015 as a major event (McPhaden, 2015). Di Lorenzo and Mantua (2016) suggest that although the 2014 El Niño fizzled, it triggered changes in the regional atmospheric pattern forcing the transition from the warm blob to more wide-spread warming along the NEP coast (Figures 1a and 1c).

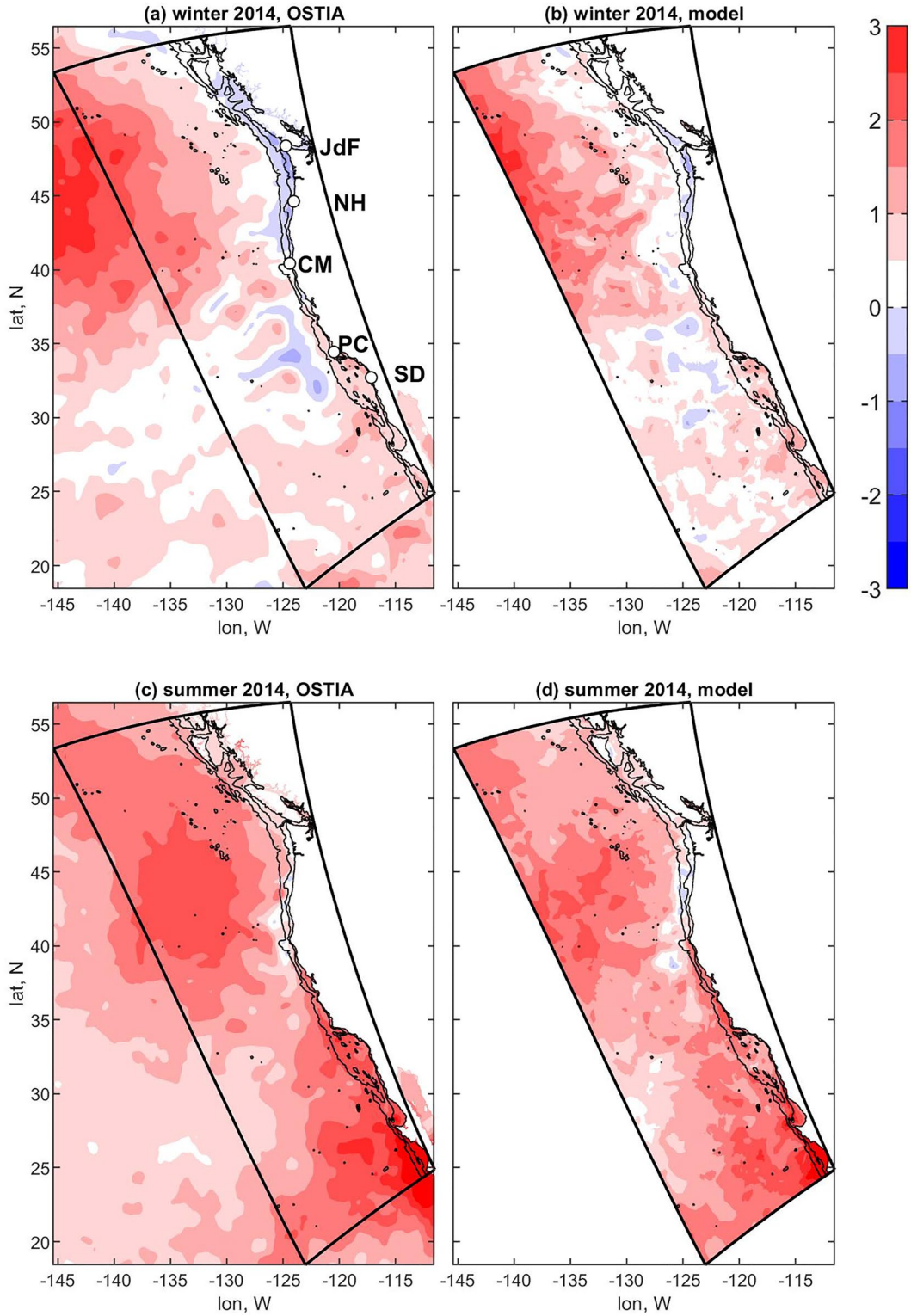

Figure 1. The 3-month averaged SST anomaly: (left) the OSTIA satellite product (Donlon et al., 2012) and (right) the model, (top) December 2013 to February 2014, (bottom) June–August 2014. The anomaly is computed with respect to the mean over the same months from the previous 5 years. The thin black contours are the coast and the 200 and 2,000-m isobaths. The thick black closed contour shows the model domain. Open circles show geographic reference points used later in the alongshore distance versus time plots (SD: San Diego, PC: Point Conception, CM: Cape Mendocino, NH: Newport hydrographic line, JdF: Juan de Fuca Strait).

In addition to the basin scale atmospheric changes that drive the El Niño oceanic response, that is, the atmospheric teleconnection mechanism (Di Lorenzo & Mantua, 2016; Schwing et al., 2002), El Niño can impact the US coastal ocean waters via the direct oceanic mechanism of coastally trapped waves (CTWs) propagating from the equatorial region to higher latitudes (Amaya et al., 2022; Frischknecht et al., 2015). These anomalies include the higher coastal SSH, the downwelling motion, and depression of isopycnal surfaces over the continental slope.

The strength of the remote CTW-driven mechanism in 2014–2016 and its relevance to the warming along the US West Coast has been a point of discussion. In California (CA), analyses of a data assimilative model state estimate (Jacox et al., 2016) and glider data (Rudnick et al., 2017) showed the depression of subsurface isopycnal levels over the continental slope in 2014 and 2015, but not as strong as in earlier major El Niño events. Zaba and Rudnick (2016) and Myers et al. (2018) point to positive anomalies in the surface heat flux offshore of CA in 2014. It is possible that a combination of the offshore surface water warming due to the anomalous downward shortwave flux and the downwelling and onshore motion due to the CTW mechanism resulted in the strong temperature anomaly over the shelf along the CA coast in summer 2014. Zaba and Rudnick (2016) conclude that "while we do not eliminate coastally trapped waves as a possible forcing mechanism, we do note that equatorial conditions were near neutral at the onset of the south CCS warming, making questionable the remote generation of coastally trapped waves." Zaba et al. (2020) analyzed a data assimilative model state estimate for CA and concluded that "downwelling anomalies persisted throughout most of 2014 and during the upwelling months of 2015," although that study did not make an attempt to connect these anomalies with the conditions to the south. Off Oregon (OR, 40.5–46.2°N), the shelf area was shielded from the warm blob by strong upwelling in summer 2014 (Figure 1c). When the southward, upwelling-favorable winds receded and the upwelling conditions relaxed in the fall, the offshore warm blob waters moved over the shelf in September 2014. Peterson et al. (2017) provide a very careful analysis of the physical and biological data along the Newport cross-shore line (NH, 44.65°N) and "leave as an open question whether the increase in SSH, decrease in equatorward velocities, and return to warm/fresh bottom conditions and negative nitrogen and chlorophyll-a concentrations in 2015 were due to the onshore return of the Blob or northward progression of a weak El Niño."

The CTW theory has been advanced using solutions of analytical and quasi-analytical linear models of the wind-forced baroclinic coastal ocean response (Brink, 1991). The direction of CTW propagation is such that the coast is on the right (left) in the Northern (Southern) hemisphere if looking in the direction of phase propagation. The CTW solutions are generally obtained using the long-wave and low-frequency approximations and exist at subinertial frequencies. The cross-shelf characteristic length scale is close to the baroclinic Rossby radius of deformation and the along-coast wavelengths are much longer than that. In limited-area theoretical or realistic numerical models, CTW at a particular location can be forced by any perturbations "upstream" of that location (upstream in the sense of the wave propagation), including the along-shore wind stress or boundary conditions. Given that existing observing systems do not have enough spatial and temporal resolution to describe the structure and evolution of CTW and that the CTW-related signal is hard to separate from other observed modes of variability, for example, local wind-driven response or surface and subsurface eddy variability over the shelf and slope (Pelland et al., 2013), the evidence of the CTW has been presented mostly using statistical methods, including time-lag correlation or coherence analyses of available coastal tide gauge or shelf velocity profile data (Allen & Denbo, 1984; Battisti & Hickey, 1984; Halliwell & Allen, 1987; Junker et al., 2019). These observation-based analyses are sometimes combined with the analyses of regional model outputs (Kurapov, Erofeeva, et al., 2017; Springer et al., 2009). Frischknecht et al. (2015) demonstrated the El Niño remote oceanic effect on the Northern American coastal regions using an ocean circulation model of the entire Pacific basin. In the Southern CA region, the variances of the anomalies in the coastal SSH and near-surface temperature and salinity on the interannual time scales were explained predominantly by the remotely forced model solution. In the Northern region (40–47°N), the remote oceanic mechanism was still dominant for SSH. The atmospheric and remote oceanic forcing mechanisms contributed equally to the near-surface temperature and salinity variability.

The main goal of this paper is to demonstrate that the El Niño signal propagated with CTW impacted shelf and slope flows off OR in 2014–2016. The anomalies related to the CTW propagation influenced the slope and shelf variability as early as in summer 2014, before the warm blob waters moved over the shelf. To the best of our knowledge, the present paper is the first modeling study focused on the Oregon shelf and slope during the 2014–2016 heat wave period. This will be done in the context of a longer, 2009–2018 analysis period.

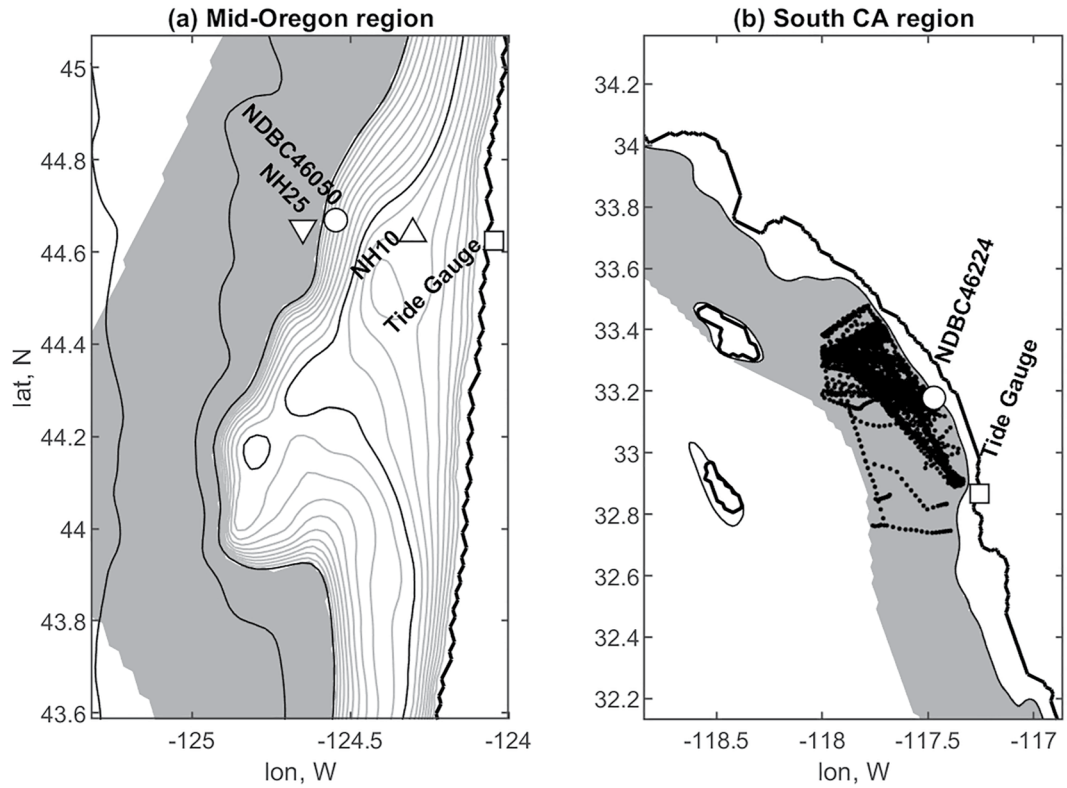

Figure 2. The in-situ observational assets: (a) the mid-Oregon region; the bathymetric contours are (black) 100, 200, 500, and 2,000 m (half-tone) every 10 m between 10 and 190 m; (b) the Southern CA region: black dots are glider profile locations; the bathymetric contour is 200 m. Gray shading in both (a) and (b): the slope band defined as the area 0–40 km offshore of the 200-m isobath. NDBC: National Data Buoy Center at NOAA; NH10 (25): the Newport Hydrographic line, 10 (25) nautical miles offshore.

Among other recent modeling efforts focused on the events of 2014–2016 along the US West Coast, Zaba et al. (2020) analyzed heat term balances in the south CA region using the 8-km resolution data-assimilative state estimate. Chao et al. (2017) used the 3-km resolution CA data-assimilative model and a higher-resolution coastal model to address the oceanic heat budget in the area near San Francisco Bay. While providing important information about the regional variability in the area, neither of these two studies diagnose CTW propagation or impact. Compared to these regional studies, the model presented below does not include data assimilation and presents an accurate dynamically and thermodynamically balanced solution most suitable for process studies.

2. Model

The Regional Ocean Modeling System (ROMS; www.myroms.org) is utilized. ROMS integrates the free-surface, fully nonlinear primitive equations for the stratified ocean under the Boussinesq and hydrostatic approximations. It uses terrain-following vertical coordinates and advanced, higher-order numerics (Shchepetkin & McWilliams, 2003, 2005). The model domain extends in the alongshore direction between 24 and 54°N (Figure 1) including part of the Mexican coastline, the entire US West Coast (32.5–47.5°N), and most of British Columbia, Canada. The grid is regular in a spherical coordinate system with the north pole rotated to (57.6°W, 37.4°N). The horizontal resolution is close to 2 km everywhere. For illustration, the model bathymetry in the central OR region is shown in Figure 2a. Forty vertical levels are distributed to resolve better the surface and bottom boundary layers. Using the ROMS vertical grid parameters (*Vstretching* = 2, *Vtransform* = 4, $\theta_s = 7$, $\theta_b = 4$, and *Tcline* = 50 m), the top 50 m are resolved by nine or more layers everywhere; over the shelf, inshore of the 200 m isobath, the bottom 20 m are represented by four or more levels. For this presentation, the vertical z-coordinate is directed upward, with $z = 0$ near the free surface, such that subsurface depths are negative. Vertical turbulence is parameterized using the Mellor-Yamada 2.5 subgrid scheme (Mellor & Yamada, 1982) with modifications by

Galperin et al. (1988) and Kantha and Clayson (1994). The model air-ocean momentum and heat fluxes are computed using a bulk flux formulation (Fairall et al., 2003). Precipitation is prescribed and evaporation is computed internally by ROMS from the latent heat flux. The tidal and non-tidal boundary conditions are set as described in Kurapov, Erofeeva, et al. (2017). To improve the stability of long-term simulations, the "sponge layer" is included by linearly increasing the horizontal viscosity from 2 $m^2\ s^{-1}$ in the interior to 200 $m^2\ s^{-1}$ at the open boundaries across a 100-km wide band. We understand that the harmonic horizontal dissipation term acts on the smallest spatial scales. The larger scales, provided at the open boundaries by the global ocean circulation model or by the regional tidal model, are relatively unaffected. Terrestrial fresh water sources include the Columbia River, Fraser River, and 15 small rivers in the Salish Sea (Giddings & MacCready, 2017).

The simulation is performed for a period from October 1, 2008 to November 25, 2018. Model analyses are done with daily averaged outputs.

To make this model suitable for studies of the remote oceanic El Niño influence on the Oregon shelf flows in 2014–2016, two modifications to our earlier model setup (Kurapov, Erofeeva, et al., 2017; Kurapov, Rudnik, et al., 2017) were required. First, the atmospheric forcing fields are provided here by the 30-km resolution ECMWF ERA5 reanalysis, in lieu of NOAA NAM (ECMWF: European Center for Medium-Range Weather Forecasts; ERA: ECMWF Re-analysis; NAM: North American Mesoscale Forecast System). In comparing the model and observed buoy wind velocities (not shown), we find that ERA5 predicts orographically intensified winds south of Cape Blanco (42.8°N) (Samelson et al., 2002) better than NAM, which is critical to the accuracy of predicting upwelling over the OR shelf north of the cape (Gan & Allen, 2005). Second, parameters for the open boundary treatment were adjusted to better match the interior solution of our regional model and the global model used for the boundary conditions, which is particularly important at the southern boundary where the El Niño-related oceanic signal will pass through. As in the earlier model version, the non-tidal boundary information is obtained from the 1/12th degree resolution global Navy HYCOM operational forecast system (HYCOM: Hybrid Coordinate Ocean Model; www.hycom.org; Cummings & Smedstad, 2013). To ensure stable and accurate integration over multiple years without boundary effects, in addition to using the "radiation + nudging" boundary conditions (Marchesiello et al., 2001), temperature T and salinity S in the regional model interior are nudged to the 1-week averaged HYCOM fields in a band along the open boundaries using the "nudging to climatology" option in ROMS. Compared to Kurapov, Rudnik, et al. (2017), nudging was enhanced and implemented in a wider band. Namely, the nudging coefficient was set to 1/5 $days^{-1}$ next to the open boundary and linearly reduced to 0 across the 150-km band.

Note that the model presented here does *not* assimilate any data. If this model reproduces the observed variability, it does so because the dynamics are forced (from the atmosphere or through the oceanic boundary conditions) and propagated correctly through the domain.

3. Methods and Data

The shelf is defined as the area inshore of the $H = 200$ m isobath. The slope band is defined as extending 40 km offshore of the 200-m isobath (see gray areas in the maps in Figure 2; the edges of the slope band are also shown in Figure 12). The bandwidth is chosen to be close to the reported slope undercurrent width (Connolly et al., 2014; Pierce et al., 2000). To track CTW, daily fields of interest will be averaged in the cross-band direction within the band limits and presented as functions of the along-slope distance from the southern boundary y and time t.

The fields of interest over the slope include the depth of the isopycnal surface $\sigma_\theta = 26.5$ kg m^{-3}, denoted $z_{26.5}$, and the subsurface along-slope velocity $v_s(y, t)$. The latter is defined by projecting the horizontal currents in a section across the slope band onto the along-band direction and averaging within the band limits in the horizontal and between $z = -300$ and -125 m in the vertical. The choice of these variables is motivated by where the core of the coastal undercurrent is expected to be found in summers (Pierce et al., 2000).

In time series analyses, the annual cycle is computed by fitting the linear combination of the mean and three harmonics with the periods of 1, 1/2, and 1/3 years to the time series. For the wind stress, the annual cycle is determined using the entire model time series (2008–2018) and for the rest of the variables using the pre-heatwave years 2009–2013. Anomalies are computed as deviations from the annual cycle.

The in-situ data locations are shown in Figure 2. The near-surface temperature time series observations are from the NOAA National Data Buoy Center (NDBC) moorings (https://www.ndbc.noaa.gov/) and the coastal sea level data are from the tide gauges (https://tidesandcurrents.noaa.gov/). The air pressure static correction is applied to the observed time series using the ERA5 sea level pressure.

Information on $z_{26.5}$ over the continental slope off OR comes from the shipboard CTD profile measurements along the Newport hydrographic (NH) line, 44.65°N (Fisher et al., 2015; Peterson et al., 2017; Risien et al., 2022; CTD: conductivity-temperature-depth). The profiles have often been collected from small boats and this operational necessity may introduce a bias toward more quiet conditions. In this paper, we use the data at NH25 (25 nautical miles from the coast, $H = 275$ m). Over the slope in southern CA, the observed $z_{26.5}$ is estimated from the Spray glider autonomous vehicle data collected along the CalCOFI line 90 (CalCOFI: California Cooperative Oceanic Fisheries Investigations). These data are part of the California Underwater Glider Network (Rudnick, 2016). While the glider line extends 500 km offshore, we retain for the analysis only profiles in the 40-km wide slope band. The data in the vicinity of Santa Catalina Island are excluded (see Figure 2b). To eliminate a large spread in $z_{26.5}$ along each glider line due to high-frequency processes, the estimates from the individual vertical profiles along each continuous glider segment are averaged and assigned to the mean segment time.

The alongshore surface shelf currents are compared to the high-frequency HF radar data (Kosro, 2005; Kosro et al., 1997). The set of hourly HF radar zonal and meridional surface velocity components collocated at the points of a 6×6 km^2 regular grid is utilized (https://cordc.ucsd.edu/). The "dilution of precision" criterion (<0.5) is used for quality control. On each day, points with less than 12 hourly values are discarded. In the remainder of the points, the observed values are daily averaged. For comparison, the daily averaged surface model velocities are sampled where the daily averaged observations are available. The meridional current component is then averaged between 43 and 46°N and inshore of the 200-m isobath to obtain the area-averaged time series, similarly to Durski et al. (2015) and Kurapov, Rudnik, et al. (2017).

To assess the accuracy of the subsurface horizontal current on the OR shelf, we utilize the Acoustic Doppler Current Profiler (ADCP) time series profiles at the NH10 hydrographic station (44.65°N, $H = 81$ m). Data collection at this location was supported from 1997 to 2012 by different observational programs led by M. Levine, P. M. Kosro, and others, with some gaps. The data from April 2013 through April 2014 are from the downward-looking 300 kHz Teledyne RDI-Workhorse ADCP supported by the Northwest Association of Networked Ocean Observing Systems (NANOOS; http://www.nanoos.org/). Unfortunately, no data are available between April 2014 and September 2014. Beginning September 24, 2014 and until present, the data have been collected by the CE02SHBP instrument (300 kHz, upward-looking Teledyne RDI-Workhorse Monitor) as part of the Ocean Observatories Initiative program (OOI, https://oceanobservatories.org/). The data are available in 4-m bins between 70 and 10 m below the surface.

4. Dynamical Forcing Anomalies

Here we show that the model oceanic boundary conditions in the south, sampled from the Navy HYCOM state estimate, exhibit anomalies that can be associated with El Niño, in particular in 2014–2015. Upwelling winds in summer 2014 and 2015 remained close to average.

At the southern boundary, variability in $z_{26.5}$ over the continental slope is consistent with our understanding of the timing of the El Niño/La Niña events (Figure 3c). The 10-m dip in 2009–2010 can be associated with the moderate El Niño, which impacted the OR coast mostly via the atmospheric teleconnection mechanism featuring anomalously strong winter winds (Durski et al., 2015). Between May 2013 and February 2016, $z_{26.5}$ exhibits a series of sharp undulations (on the order of 20 m) and gradual deepening from $z_{26.5} = -250$ to -275 m as a manifestation of El Niño, after which the isopycnal surface rebounds back to -250 m in the sharp La Niña transition. The interior model solution (black line in Figure 3c) follows closely the boundary conditions (half-tone line). The model setup propagates effectively the global model signal into the regional model interior.

In OR (Figure 3a), upwelling-favorable winds in spring-summer 2014 and 2015 were close to normal. Weaker than normal downwelling-favorable winds are found along the OR shelf in October 2013 through January 2014 illustrating the coastal expression of the warm blob basin-scale atmospheric conditions. Alongshore winds off Southern CA (Figure 3b) are on average upwelling-favorable year-around and are considerably weaker than off OR (note the ranges on the vertical axes in Figures 3a and 3b are different).

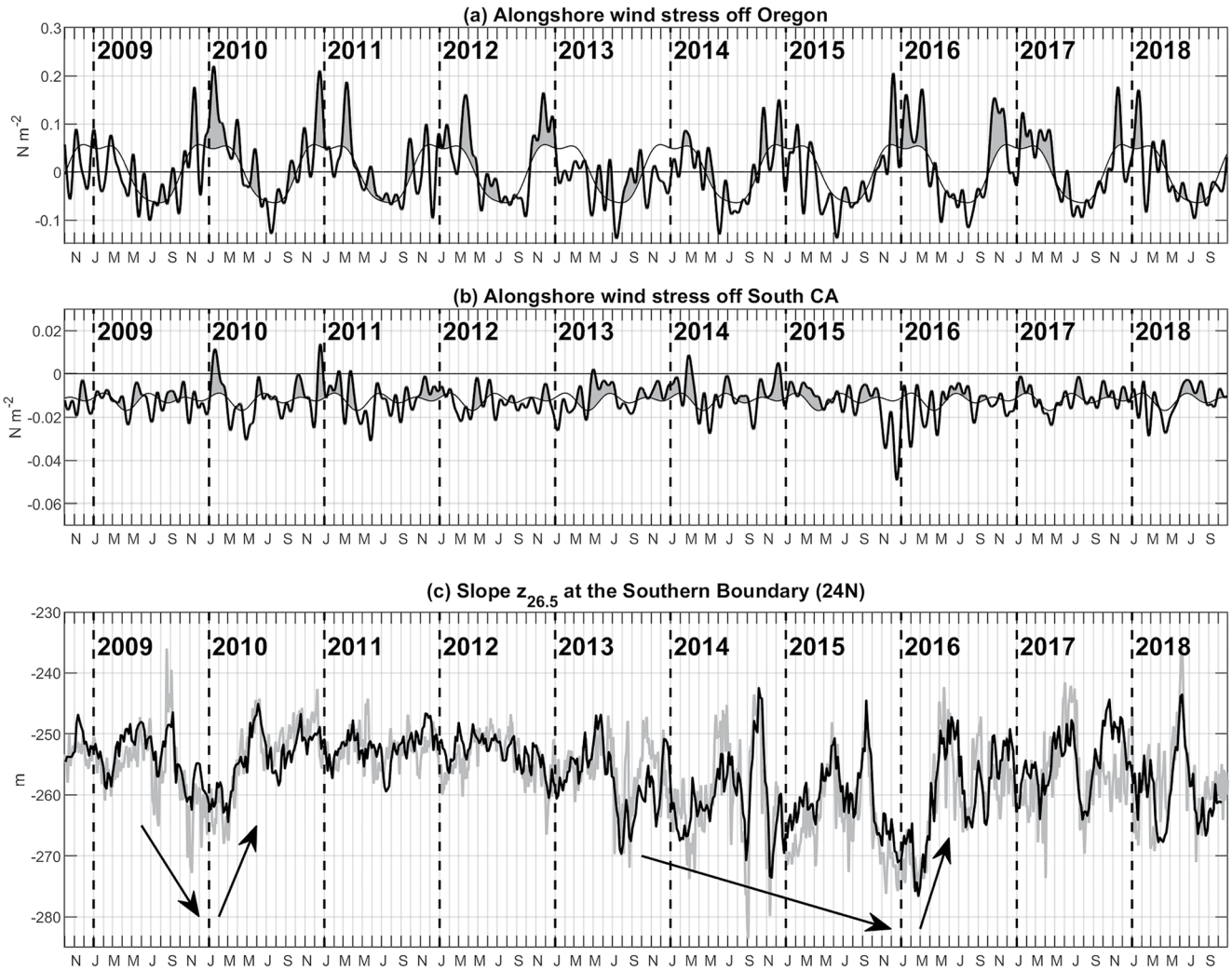

Figure 3. Selected model forcing time series: (a) alongshore wind stress offshore of Oregon, averaged between 43 and 45°N and 0–100 km offshore (the alongshore direction is defined as northward), (b) alongshore wind stress offshore of Southern CA, averaged between 32 and 34°N and 0–100 km offshore (the alongshore direction is defined as 23° to the west from the true north). In (a) and (b), the thick line is the 30-day low-pass filtered stress; the thin line is the annual cycle based on 2009–2018, the shade shows the positive anomalies from the annual cycle. (c) Slope averaged $z_{26.5}$: (half-tone) the southern boundary conditions and (black) the interior solution averaged in the along-slope direction between 0 and 100 km from the southern boundary. Arrows show tendencies during the 2009–2010 and 2014–2016 El Niño/La Niña transitions.

5. Model-Data Comparisons

A series of model-observation comparisons presented here confirm that the model reproduces correctly the regional and shelf dynamics on temporal scales from several days to seasonal and interannual.

As seen in the 3-month averaged model and observed SST anomalies, the model reproduces the eastern half of the offshore warm blob, cut off by the model offshore boundary in winter 2013–2014 (Figures 1a and 1b). By summer 2014 (Figures 1c and 1d), the warm anomaly is visible all along the coast, and the spatial variability is similar in the model and satellite SST. Conditions remain close to average in the coastal area off OR where local upwelling protects the shelf.

Comparisons of the model and observed near-surface shelf T time series (Figure 4) show that the 10-year integration proceeds without biases or erroneous trends both in OR and Southern CA. Again, it is important to note that this result is obtained without the assimilation of any data inside the domain or adjustments to the heat flux to match SST, speaking to the high level of model skill and the quality of the ERA5 atmospheric fields. In OR (Figure 4a), the model is intermittently warmer than observations in winter 2013–2014, by up to 1.5°C. Also,

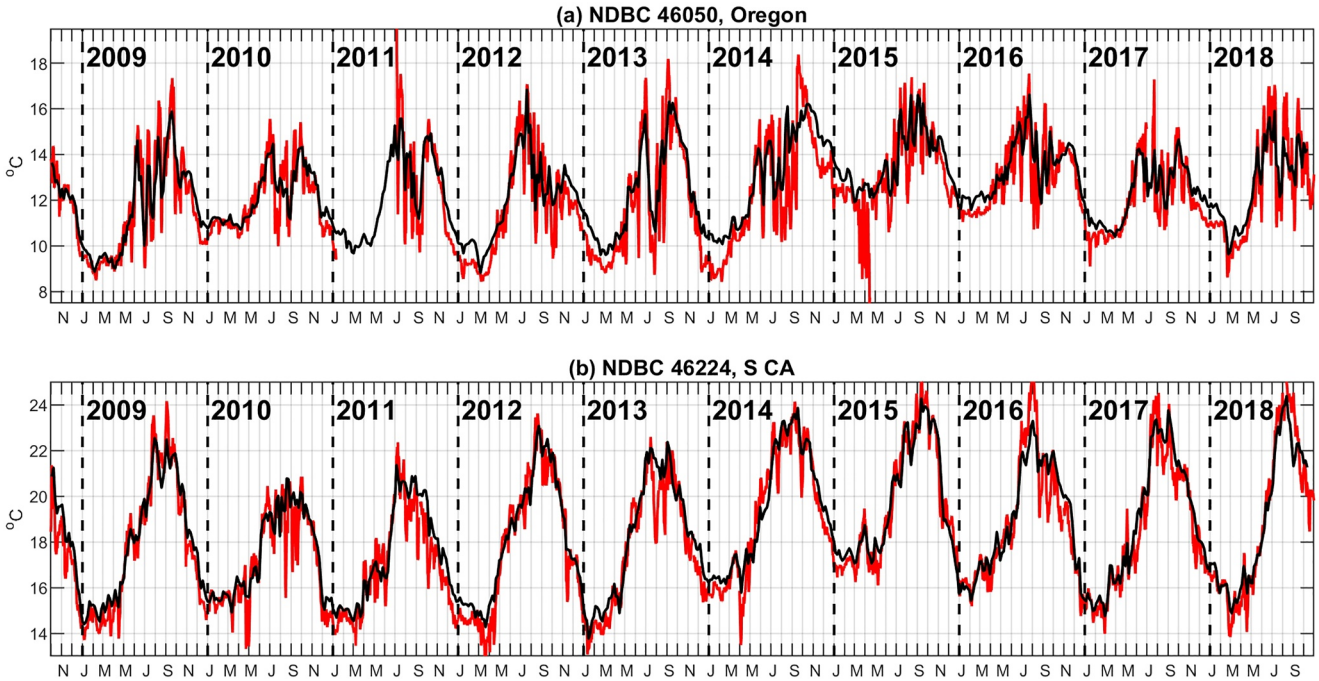

Figure 4. Time series of daily averaged (black) model and (red) observed near-surface temperature at the shelf mooring locations: (a) NDBC 46050, Oregon, (b) NDBC 46224, Southern CA.

variations in summers associated with the onshore and offshore upwelling front displacement in response to the alongshore winds are sometimes not as strong in the model as in the data, suggesting that the model upwelling front is more diffused than the real one. Despite these shortcomings, the model correctly reproduces the 3°C increase from January 2014 to 2015 and then the gradual recovery of the winter temperatures to the pre-heatwave

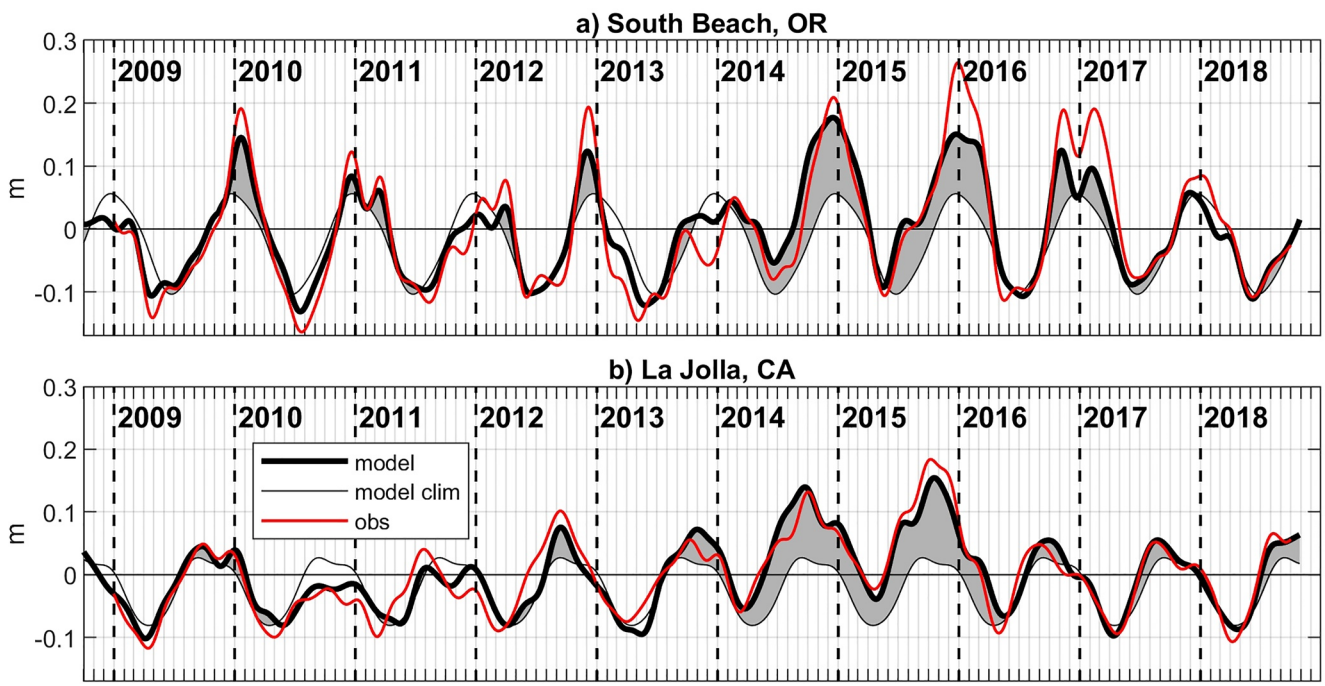

Figure 5. Time series of the 90-day low-pass filtered coastal sea level, shown with respect to the Mean Sea Level at each location: (thick black) model, (thin black) model annual cycle based on 2009–2013 and (red) observed, tide gauge: (a) South Beach, OR, (b) La Jolla, CA. Model positive anomalies are shaded.

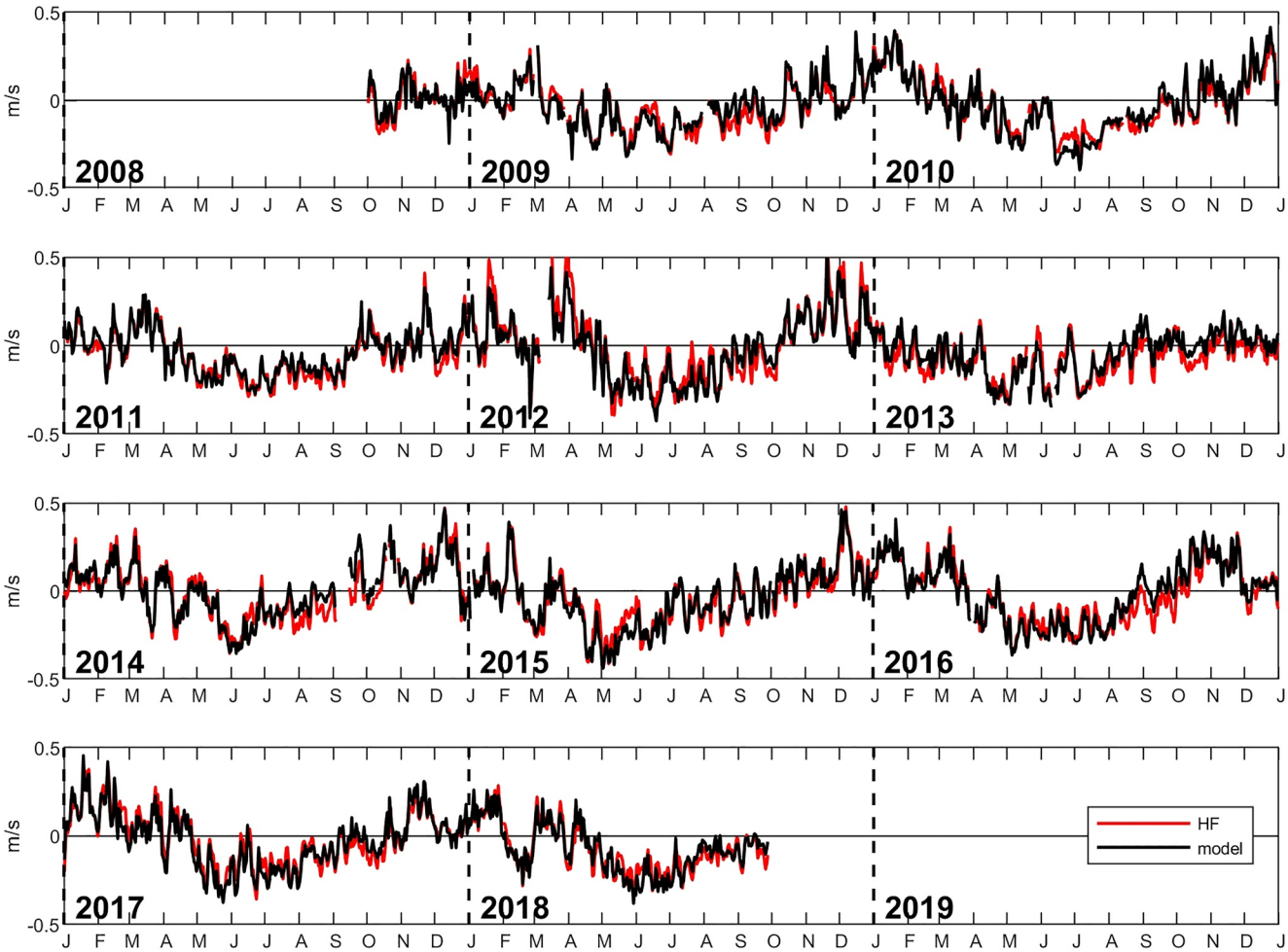

Figure 6. Time series of area-averaged, daily averaged (black) model and (red) HF radar observed surface alongshore current component off Oregon. The averaging area is between 43 and 46°N and between the coast and the 200-m isobath.

level in 2016–2018. In Southern CA (Figure 4b), the increase in the winter temperatures happened earlier than in OR, with the 2°C jump from January 2013 to 2014.

The 90-day low-pass filtered coastal sea level time series compares well between the model and tide gauge observations both in OR and CA (Figure 5). In response to the 2009–2010 El Niño that impacted the US West Coast mostly via the atmospheric teleconnection, the large positive anomaly is found in OR, but not in Southern CA. The 2014–2016 El Niño exhibits strong positive SSH anomalies at both locations, peaking at 0.15 m. The positive anomaly in Southern CA was already evident in September 2013. If that positive anomaly did propagate to OR, it was negated by the weak SSH response to anomalously low northward alongshore winds between October 2013 and January 2014 (see Figure 3a). During this period, the negative anomaly is much stronger in observations than in the model. In winters 2015–2016 and 2016–2017, the observed positive anomalies in OR are stronger than modeled, while in CA the model and observations are in tight agreement.

The time series of model and HF radar daily averaged, shelf-averaged meridional currents are split into several lines to emphasize the model accuracy on a wide spectrum of temporal scales, from the weather-band (2–20 days) to seasonal and interannual (Figure 6). The model using the ERA5 wind forcing reproduces observed variability better than our earlier solution, in which the NAM winds were used, particularly in 2011 and 2014 (cf. fig. 3 in Kurapov, Rudnik, et al., 2017). We also verified that the model alongshore current is consistent with the HF radar data in Central and Southern CA (not shown), where the performance over the 10-year record is similar to that reported in Kurapov, Rudnik, et al. (2017).

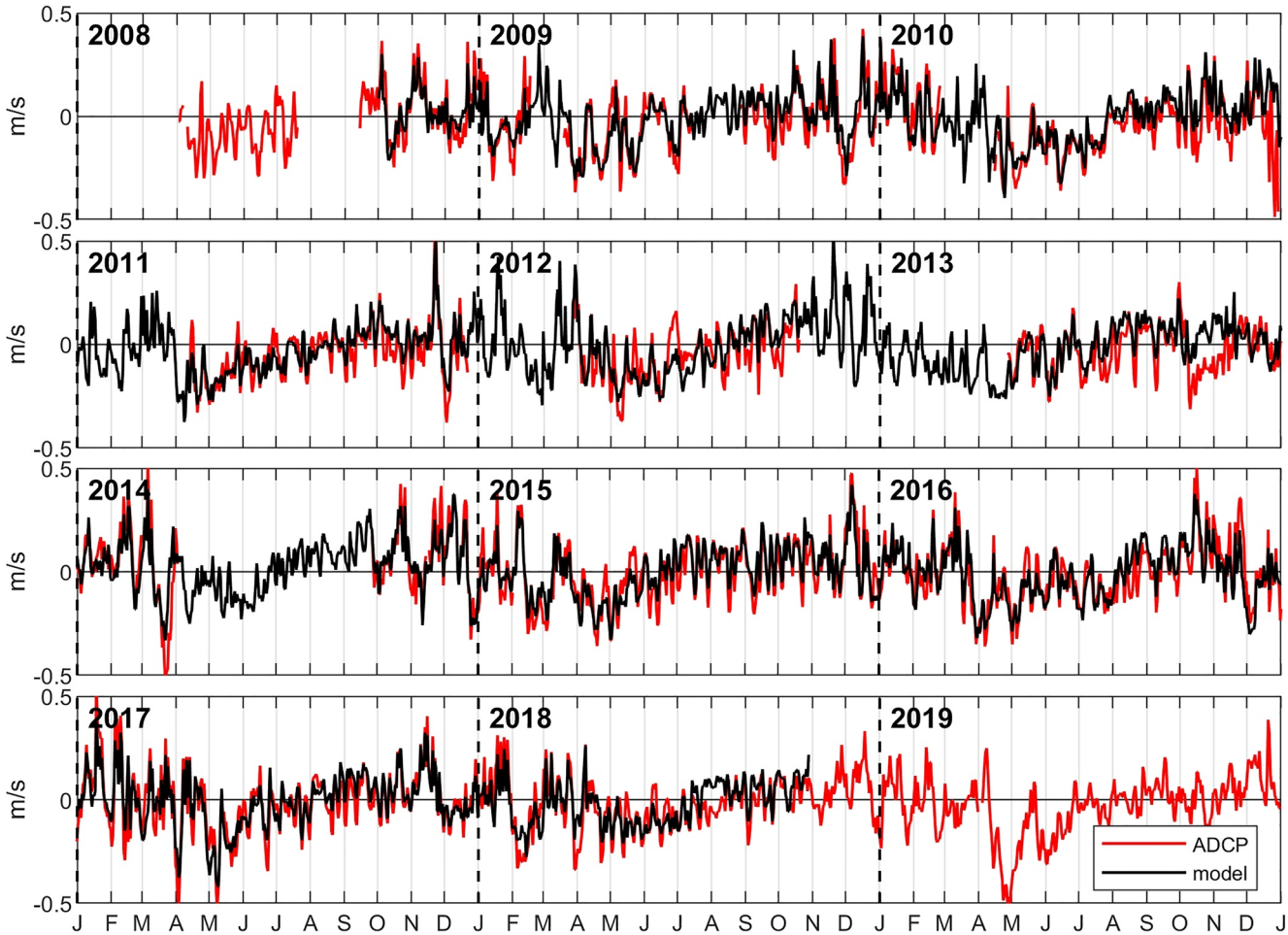

Figure 7. Time series of the daily averaged meridional current component at the NH10 location, averaged in the vertical between 60 and 70 m below the surface: (red) ADCP data and (black) model.

The accuracy of the subsurface current on the OR shelf is assessed by using the NH10 ADCP meridional current data averaged between 60 and 70 m depths (Figure 7). The model reproduces the observed variability over the entire 10-year period very well, except for episodes in December 2010 and October 2013. Overall, no systematic biases or trends are found. Since the ADCP observations are not available within the bottom 10 m, this comparison mostly applies to the flows at the top of or immediately above the bottom boundary layer.

Over the slope, the model reproduces qualitatively correctly the seasonal and interannual variability in $z_{26.5}$ both in OR and southern CA (Figure 8). The isopycnal level rising in summers in both regions is a signature of the seasonal upwelling. In Southern CA, summer peaks and winter troughs in 2014–2015 are about 20 m lower than in 2009–2013 and 2017–2018, consistent with earlier findings (Zaba & Rudnick, 2016) and also with the scale of El Niño-related anomalies at the model southern boundary (see Figure 3c). Off OR (Figure 8a), the summer peaks are about 40 m deeper than those in 2009–2013 and are not as full, as the abrupt downwelling motion happens earlier than usual, in July–August. In the winters influenced by El Niño, including 2009–2010, 2014–2015, and 2015–2016, the values are relatively lower than in other winters studied. During these winters, on some days, observation and model analyses return no $z_{26.5}$ value as the selected isopycnal surface retreats well below 275 m.

6. Slope Properties: The Annual Cycle and 2014–2015 Anomalies

Revealing the CTW-like propagating patterns may possibly be easier using subsurface oceanic fields over the slope than surface fields. For instance, in our experience, if the coastal SSH is plotted as a function y and t, the CTW propagating patterns are mixed up with the large-scale alongshore patterns that can possibly be the

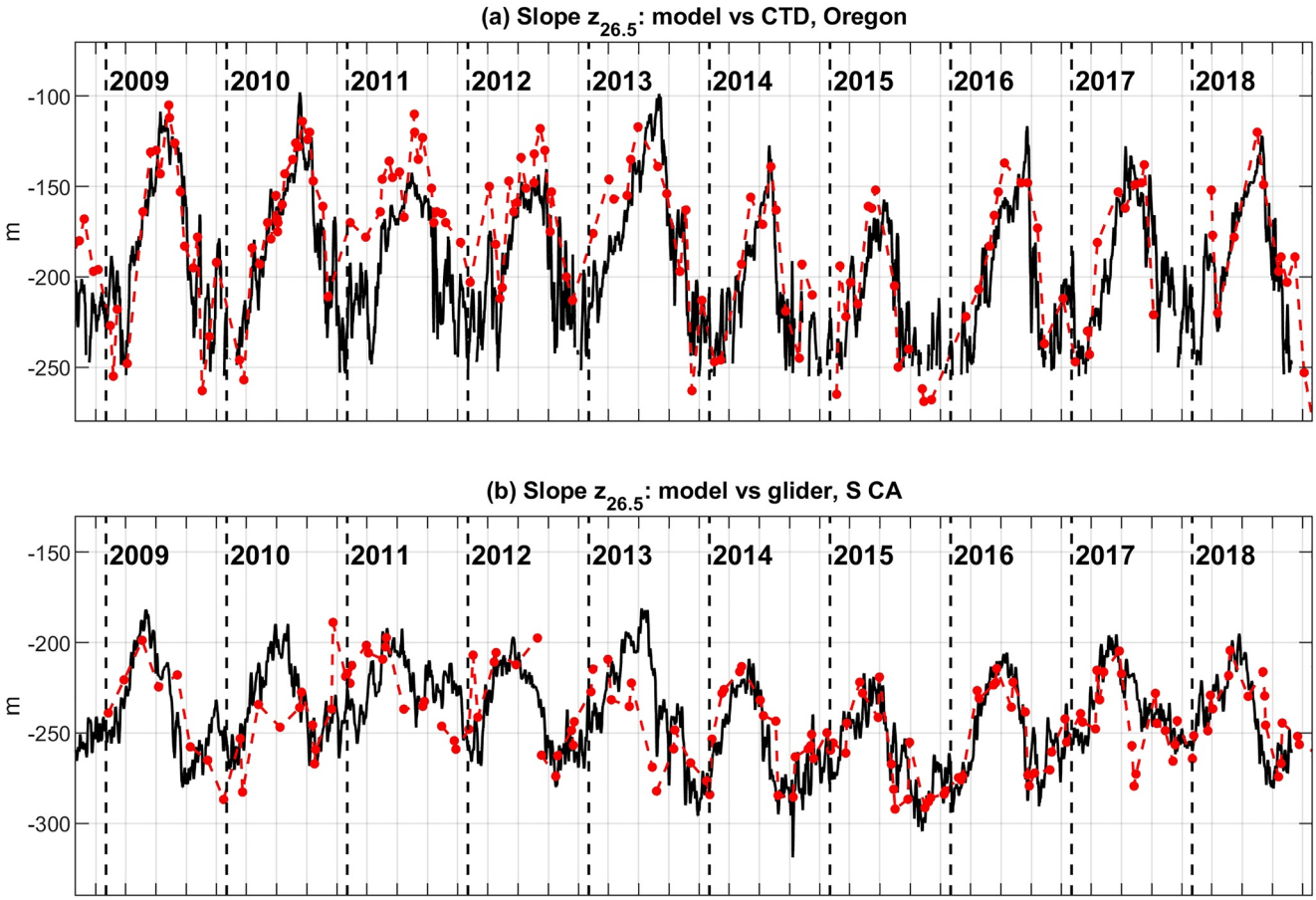

Figure 8. Time series of slope $z_{26.5}$ comparing (black) daily averaged, cross-slope-band averaged model and (red) observations: (a) ship CTD observations at the NH25 location off Oregon coast, (b) glider data off the coast of Southern CA. See Figure 2 for observation locations. Horizontal tick marks are for March 1, June 1, September 1, and December 1 each year. Note that the ranges of values on the vertical axes in (a) and (b) are the same.

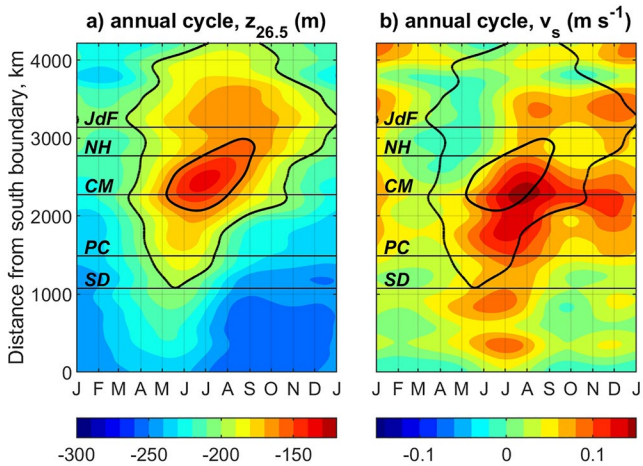

Figure 9. The annual cycle in the along-slope properties: (a) $z_{26.5}$, (b) v_s. Black contours are $z_{26.5} = -200$ and -160 m. Horizontal lines are San Diego (SD, 32.7°N), Point Conception (PC, 34.4°N), Cape Mendocino (CM, 40.4°N), Newport, OR (NH, 44.6°N), and Juan de Fuca Strait (JdF, 48.4°N) (see Figure 1a).

instantaneous local response to large-scale winds or the signatures of barotropic Kelvin wave propagation (Davis & Bogden, 1989). In our analyses, we initially attempted to track CTW using $z_{26.5}(y, t)$. The choice of variable was natural as we had already used it to analyze the El Niño oceanic forcing anomaly (see Figure 3c) and discussed the model and observed anomalies in CA and OR (see Figure 8). We want to see if the anomaly forced at the model southern boundary propagates as far up north as OR. However, as is described below, the CTW $z_{26.5}$ patterns are complicated by the presence of nearly stationary features that require explanation. The uninterrupted CTW propagation will be seen better in the along-slope subsurface velocity $v_s(y, t)$ that is defined without reference to particular isopycnal layers (see Section 3).

The annual cycle in $z_{26.5}$ (Figure 9a) shows values within the vertical limits utilized in the definition of v_s (i.e., between -300 and -125 m). The summer upwelling pattern is apparent all along the slope, with the shallowest values, $z_{26.5} > -160$ m, in Northern CA and OR. The peak values are found in the south earlier than in the north, which is confirmed by the glider data analyses (Kurapov, Rudnik, et al., 2017). In the annual cycle in v_s (Figure 9b), peak summer values correspond to the undercurrent. These lag the peaks in $z_{26.5}$ by about a month between San Diego (SD) in Southern CA and the NH line in OR, which is consistent with the theory explaining the undercur-

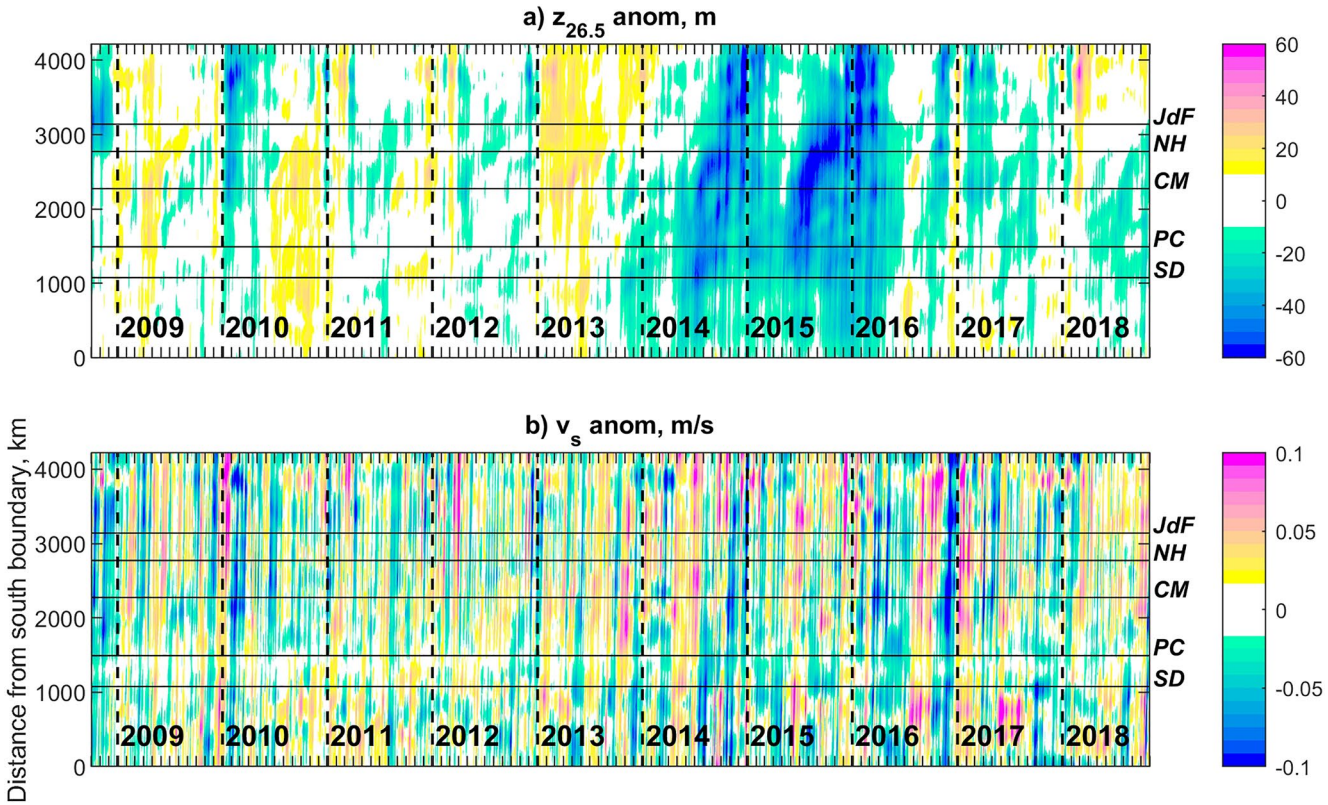

Figure 10. The anomalies in the along-slope properties in time versus along-slope distance, for the entire study period: (a) $z_{26.5}$, (b) v_s. A Gaussian low pass filter (100-km correlation scale) is applied in the along-slope direction. Horizontal lines are for San Diego (SD, 32.7°N), Point Conception (PC, 34.4°N), Cape Mendocino (CM, 40.4°N), Newport, OR (NH, 44.6°N), and Juan de Fuca Strait (JdF, 48.4°N).

rent as part of the slow planetary baroclinic wave response following the onset of the coastal upwelling conditions (Samelson, 2017). Our model also shows a weaker peak in winter in Mexico (Figure 9b, below the SD line), where the biannual component was reported to dominate the seasonal variability in the slope undercurrent (Gómez-Valdivia et al., 2017).

The anomalies in $z_{26.5}(y, t)$ and $v_s(y, t)$ are presented in Figure 10 for the entire study period to see how unique the 2014–2016 anomalies are compared to the rest of the record. To remove eddy effects (Molemaker et al., 2015; Pelland et al., 2013), a Gaussian filter with correlation length of 100 km is applied along y. $z_{26.5}$ exhibits negative anomalies during the El Niño period that are connected to the southern boundary anomalies. These are uniquely strong if the entire time series is considered. Compared to this, the winter 2010 anomaly related to the weaker El Niño looks very intermittent. The patterns of uninterrupted CTW propagation from 24 to 54°N are much clearer in the v_s. What may be perceived as almost vertical lines in this plot are actually propagating patterns with speeds near 2.5 m s^{-1} characteristic of non-dispersive dominant mode CTW in a range of relatively fast (several days to intraseasonal) frequencies. The estimate of 2.5 m s^{-1} is on the same order as the phase speed predicted by the simplest analytical model of baroclinic CTW for a linearly stratified, flat bottom case: $\pi^{-1}NH$, where N is the buoyancy frequency (Kurapov et al., 1999, 2002). It is also close to theoretical estimates using more realistic bottom profile and stratification (Illig et al., 2018) and to observation-based coastal sea level coherence phase estimates (Kurapov, Erofeeva, et al. (2017)).

To see the fast propagating CTW patterns better, we stretch the plot and show only 2014–2015 (Figure 11). To increase the contrast presenting $z_{26.5}$, the range of the values in Figures 11a and 11b is changed compared to Figure 10a and shows only negative values. If the Gaussian alongshore low-pass filter is not applied to $z_{26.5}$ (Figure 11a), small-scale patterns of stronger or weaker anomaly show up as nearly stationary or drifting slowly to the north. These correspond to the undercurrent instabilities, flow separations, and eddies emerging over the slope that contribute to widening areas of deeper $z_{26.5}$. If these eddy-like patterns are filtered (Figure 11b), the

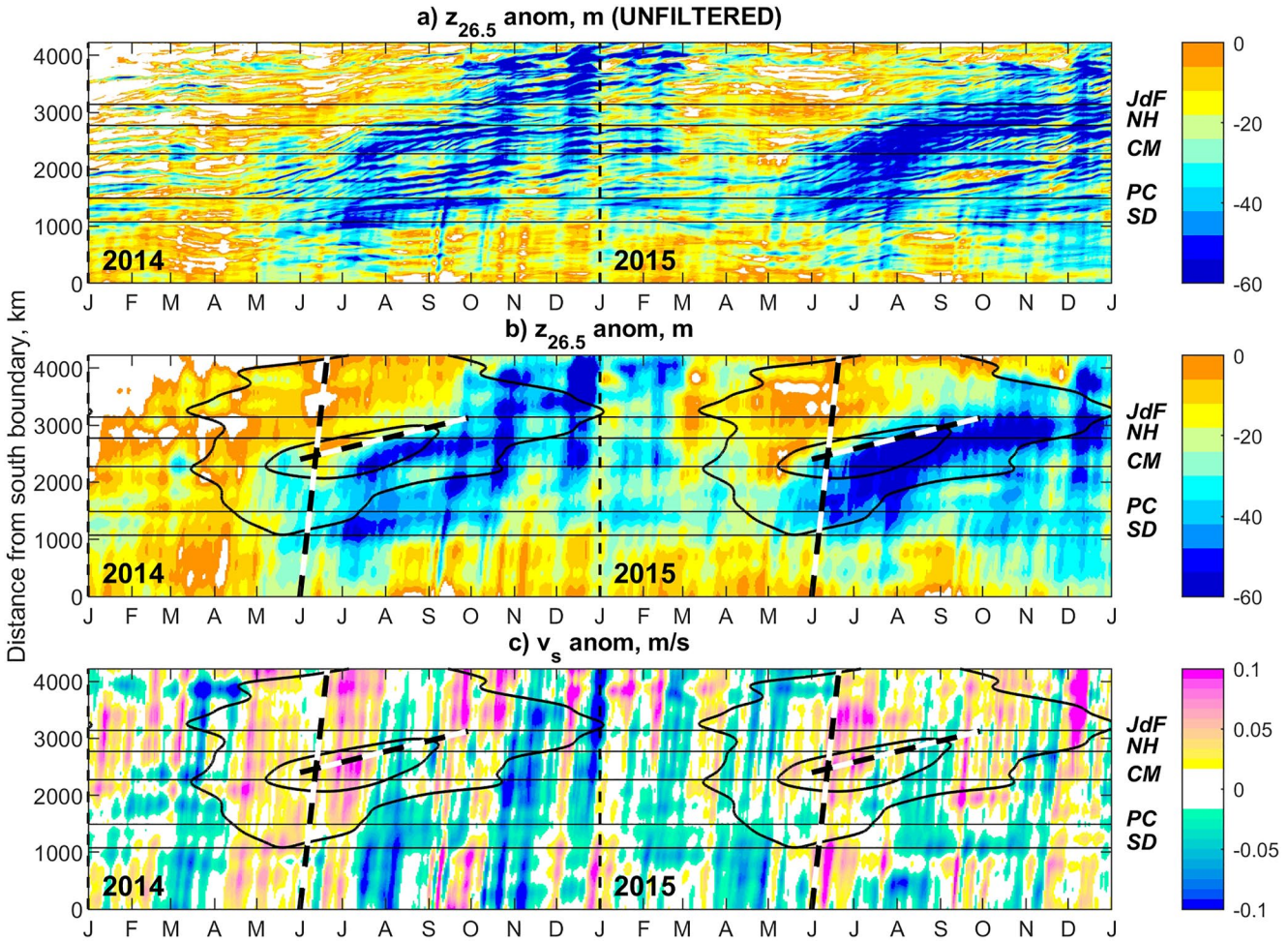

Figure 11. The anomalies in the along-slope properties in time versus along-slope distance, a close-up on 2014–2015: (a) $z_{26.5}$, without the low-pass filter in the alongshore direction, (b) $z_{26.5}$ (filtered), (c) v_s (filtered). Black contours show the annual cycle in $z_{26.5}$ (−200 and −160 m) from Figure 9a. Black-white guide lines are 2.5 and 0.07 m s^{-1}, characteristic of the CTW speed and the along-slope current, respectively. Horizontal lines are San Diego (SD, 32.7°N), Point Conception (PC, 34.4°N), Cape Mendocino (CM, 40.4°N), Newport, OR (NH, 44.6°N), and Juan de Fuca Strait (JdF, 48.4°N). In (a)–(b), the white areas are the positive anomalies.

CTW patterns are revealed in $z_{26.5}(y, t)$ but the plot cannot be explained as simply CTW propagation. In particular, deep anomaly patterns persist between SD and NH in July 2014 and 2015. These are apparently deeper than the patterns at the southern boundary and travel alongshore with speeds <0.1 m s^{-1}. They slow down as summer progresses and become nearly stationary by fall. In animations of the daily maps of $z_{26.5}$ we see episodes of the fast propagation of the depressions along the edge of the shelf break. When this happens and if the undercurrent shows instabilities or flow separation around topographic features, the depression is entrained into those eddy-like features that can extend across the entire 40-km slope band and travel along the slope with speeds close to v_s. Some of them grow and eventually separate as California undercurrent eddies or "cuddies" (Pelland et al., 2013). For illustration, in the map of $z_{26.5}$ on July 15, 2014 (Figure 12a), a band of deeper $z_{26.5}$ extending along the slope is characteristic of the CTW pattern. On August 26, 2014 (Figure 12b), large separation areas are apparent along the slope. The slope current generally follows their edges and the isopycnal surface is depressed inshore of the separation zones. The depression occupies a wider area within the slope band. So, nonlinear advective processes contribute to the appearance of the near-stationary patterns in the slope-averaged $z_{26.5}(y, t)$.

The westward planetary wave propagation also contributes to the widening of the zone of lower $z_{26.5}$ across the slope and may explain the slow-down of the nearly stationary patterns late in summer apparent in Figure 11b. The offshore propagating patterns emerge if a long enough temporal filter, for example, a 3-month running average, is applied to $z_{26.5}(lon, lat, t)$ (Figure 13). The offshore propagating patterns are evident both in the annual cycle and

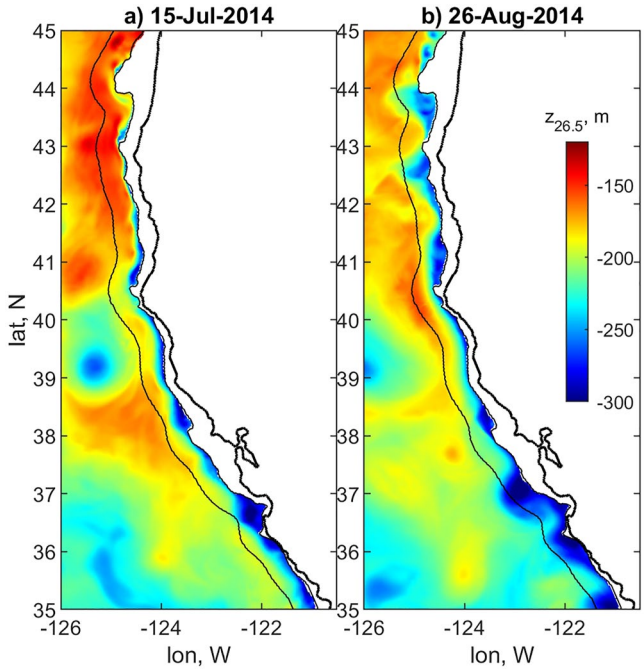

Figure 12. Daily averaged $z_{26.5}$ showing both the effects of CTW and the widening due to the local nonlinear effects: (a) July 15, 2014, (b) August 26, 2014. The black contours show the edges of the 40-km wide slope band, offshore of the 200-m isobath.

the anomalies. The propagation speeds, close to 0.01 m s^{-1} offshore of OR and 0.02 m s^{-1} in Southern CA, are consistent with the first mode baroclinic Rossby wave speed estimates (Aoki et al., 2009).

Returning to the discussion of the slope *y*-*t* patterns, periods of sustained positive anomaly in v_s, reaching 0.1 m s^{-1}, precede or coincide with the emergence of the deep non-CTW $z_{26.5}$ anomaly patterns between SD and JdF in spring and summer 2014 and 2015 (Figure 11c). The word *sustained* is key here, as we can find velocity anomalies of a similar magnitude outside 2014–2015 if the entire 10-year record is considered (see Figure 10b).

7. Velocity Anomalies on the Shelf

Using idealized, along-shore uniform models, CTWs are described as a superposition of mixed barotropic-baroclinic cross-shore versus vertical modes (Brink, 1991, 2006; Musgrave, 2019; Wang & Mooers, 1976). In the dominant mode, the slope and shelf velocities are positively correlated. Positive velocity anomalies propagating as CTW and revealed in our model solution over the slope, particularly in summers 2014 and 2015, must be accompanied by the positive alongshore velocity anomalies over the shelf.

Vertical profiles of the model monthly averaged alongshore and cross-shore horizontal velocity components at the NH10 location, for May–September 2014 and 2015, are shown in Figure 14. For this analysis, the alongshore direction is defined to be 24.3° to the east from true north, determined as the direction of the major axis of variance ellipse of the depth-averaged model current vector (Kurapov et al., 2005; Oke et al., 2002). In May and June 2014 (Figures 14a and 14b), the alongshore current is close to average showing the sheared southward flow. In July 2014 (Figure 14c), the current is reduced abruptly compared to June and is much weaker than the 2009–2013 average. The vertical shear in the alongshore current also became smaller than average in July 2014, suggesting that the isopycnal surfaces flattened in the cross-shore direction. A similar sharp drop in the southward alongshore current is seen in the model May–July 2015 (Figures 14f–14h). Conditions return closer to average by September in each year. The near-bottom cross-shore current is close to average in May 2014 (Figure 14k). Starting in June and through September (Figures 14l–14o), the near-bottom current anomaly is negative (toward offshore) in the bottom boundary layer. At the same time, supported by the upwelling-favorable winds, the near-surface offshore transport is close to average. Similarly, in June-July 2015 (Figures 14q–14r), the near-bottom cross-shore currents exhibit the negative (offshore) anomaly. Overall, the passing of the El Niño related CTW is associated with the weaker alongshore southward current and the less upwelling-favorable or more downwelling-favorable near-bottom transport, but not necessarily a weaker near-surface offshore transport.

We do not have observations to confirm the weakened cross-shore transport in the bottom boundary layer in summers 2014 and 2015, but we can revisit the NH10 ADCP and HF radar data to confirm the positive anomaly in the alongshore flow. First, we return to using the NH10 ADCP and model velocities averaged between the depths of 60–70 m (see Figure 7). From those, the monthly averaged eastward *u* and northward *v* velocity components are computed for each month in 2009–2018. Then, *u* is plotted against *v* separately for May, June, July, and August (Figure 15, top plots: model, bottom plots: observations). In the observational plots, *v* was algebraically the largest (i.e., the least negative or most positive) or near the largest in May–August 2015 (red triangles). There is a sharp transition from June to July to larger *v*. The model shows qualitatively similar behavior in 2015. In 2014, for which the model estimates are only available (green squares), the current is southward and close to the average in June. However, the model shows a sharp transition to the northward current in July, similar to 2015.

By looking at Figure 7, where observations continue into 2019, we see that 2019 may represent yet another year with the sharp weakening of alongshore near-bottom current between June and July. While the 2019 analysis is beyond the scope of this paper, we note for future reference that this effect may be associated with the 2019–2020 marine heat wave (Chen et al., 2021).

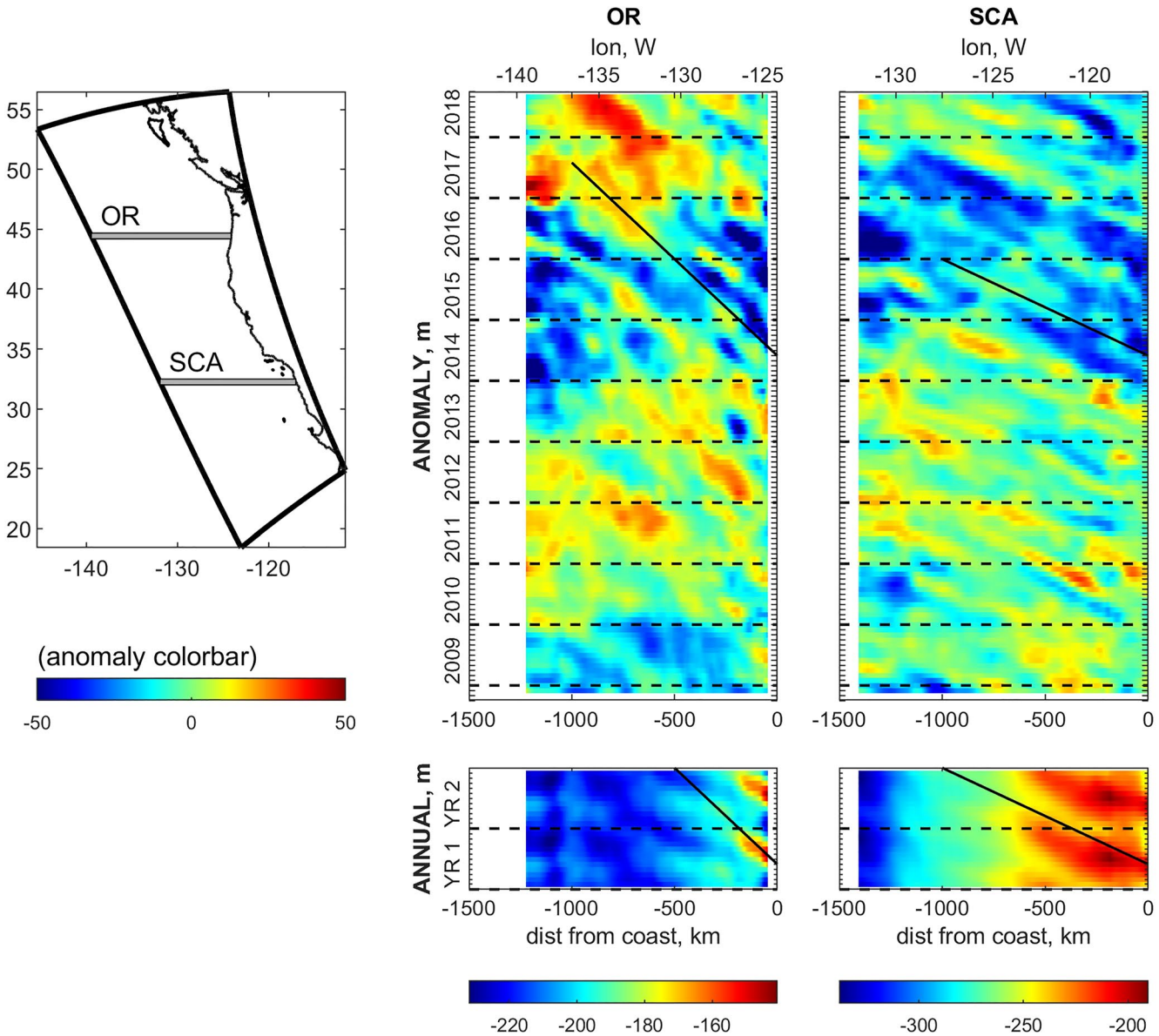

Figure 13. Offshore propagation of slope $z_{26.5}$ disturbances, units are meters: (bottom) annual cycle (2 years shown), (top) anomaly from the annual cycle. Analyses are based on the 3-month running average model outputs saved monthly and the annual cycle is computed using 2009–2013. Averaging in the meridional direction is over 0.5° bands, shown in the map on the left. OR: 44.2–44.7°N, SCA: 32–32.5°N. The guide lines are 0.01 m s^{-1} for Oregon (OR) and 0.02 m s^{-1} for Southern CA (SCA).

Next, we use the HF radar surface current data to confirm the sharp transition to weaker southward current conditions from June to July in 2014 and 2015. The monthly average values for June, July, and August of each year are obtained from the shelf-averaged meridional current time series presented earlier in Figure 6. In Figure 16, the values for each month are plotted as a function of the year, separately for the HF radar data and the model. The model suggests that 2014 and 2015 were the only years in the 10-year record with the abrupt transition to much lower and anomalous currents from June to July (as emphasized by the vertical arrows in the plot). The HF radar data analysis shows qualitatively the same dynamics, although the transition from June–July 2014 is not as dramatic in the data as in the model. Still, qualitatively consistent between the observations and the model, the July 2014 and 2015 alongshore currents are the two lowest among all the July estimates and the June to July transitions in 2014–2015 are the two strongest in the 10-year record.

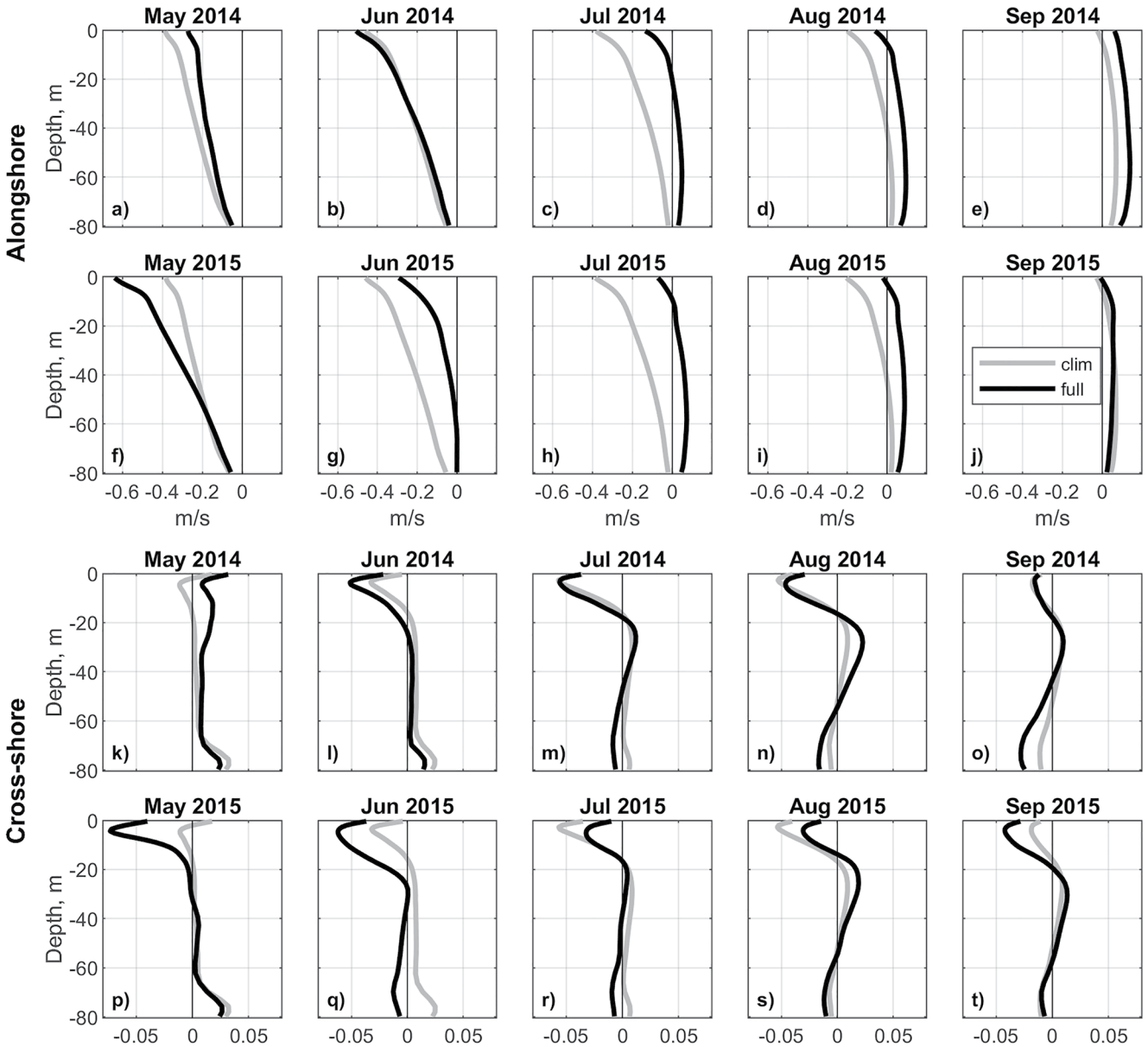

Figure 14. Vertical profiles of the model monthly averaged (rows 1 and 2) alongshore and (rows 3 and 4) cross-shore velocity components at the NH10 shelf location in Oregon. (Black) monthly averaged (half-tone) climatology based on monthly means in 2009–2013. The alongshore direction is defined as the direction of the major principle component of the depth-averaged current at this location, at 24.3° to the east from true north.

8. Conclusions

The oceanic CTW mechanism did have a measurable impact on the currents and hydrographic anomalies over the shelf and slope off Oregon during 2014–2016 that can be associated with El Niño. Among the model variables analyzed, the CTWs are best seen in the anomalies of v_s, the along-slope velocity component averaged across the slope and between $z = -300$ and -125 m. The CTW propagate uninterrupted from the southern to northern boundaries of our domain, between 24 and 54°N. v_s is anomalously large in spring-summer 2014 and 2015, by up to 0.1 m s^{-1}. CTW patterns are also evident in the $z_{26.5}(y, t)$ anomaly maps. However, those maps cannot be interpreted solely as CTW propagation and point to the importance of nonlinear advective effects enhanced by the increased slope currents. Zones of slower, nearly stationary strong negative $z_{26.5}$ anomalies emerge along portions of the US West Coast at the time of intensive CTW anomaly propagation only in the El Niño years. They are deeper than the anomalies defined by the southern boundary conditions, in part because $z_{26.5}$ represents the

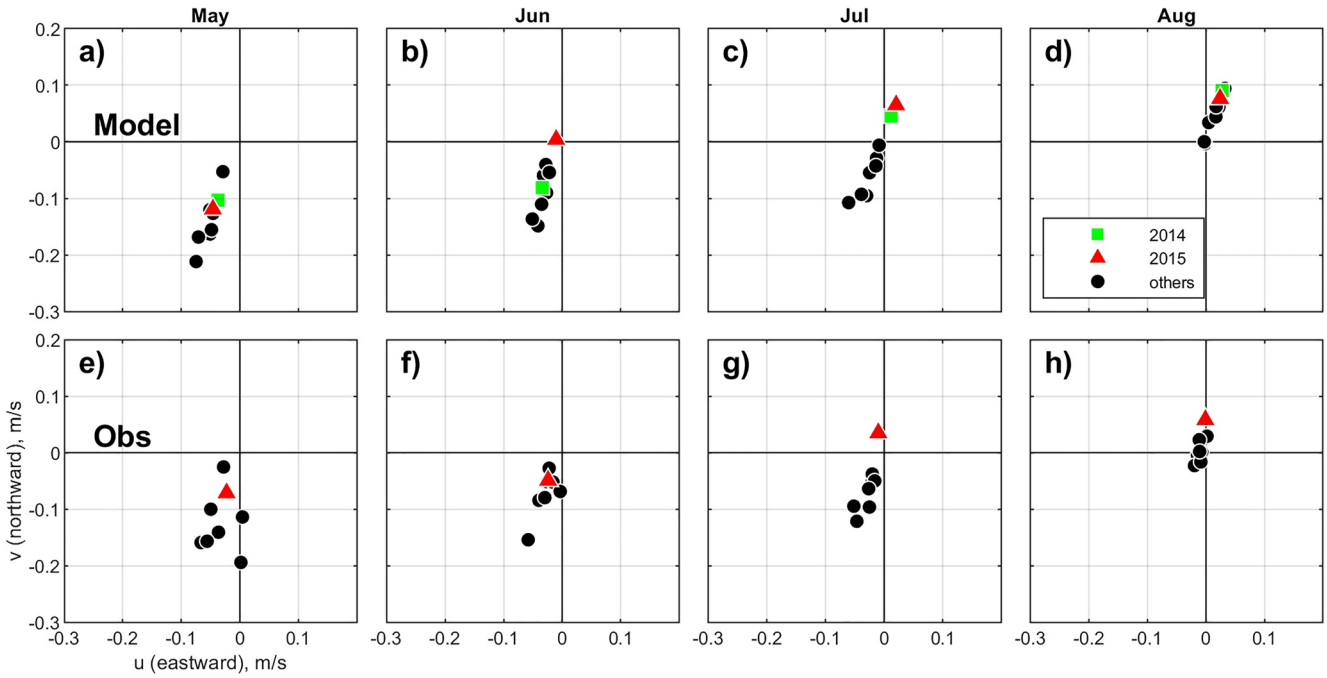

Figure 15. Monthly averaged eastward versus northward model current components at the NH10 location, for the depths between 60 and 70 m, that is, 11–21 m above the bottom. (Left to right) May through September; (top) model, (bottom) ADCP observations. 2014: green squares, 2015: red triangles, all other years: black circles.

slope-band averaged quantity, and the apparent deepening is mostly due to the widening of the low $z_{26.5}$ anomaly across the band. The wider, flow-separation areas emerge over the slope because of the undercurrent instability, separations at the topographic irregularities, and eddy detachment from the slope. In these areas, $z_{26.5}$ adjusts to the baroclinic velocity field and is generally lower on the inshore side of the slope current path. On the slower, intra-seasonal time scales, planetary wave dynamics also contribute to the offshore $z_{26.5}$ anomaly propagation.

The CTW-like slope current anomalies revealed in v_s are a part of the shelf-wide El Niño impact. In summers 2014 and 2015, the southward alongshore current is weakened or reversed over the shelf despite the upwelling-favorable winds being close to average. The model also shows the downwelling anomaly in the near-bottom cross-shore current.

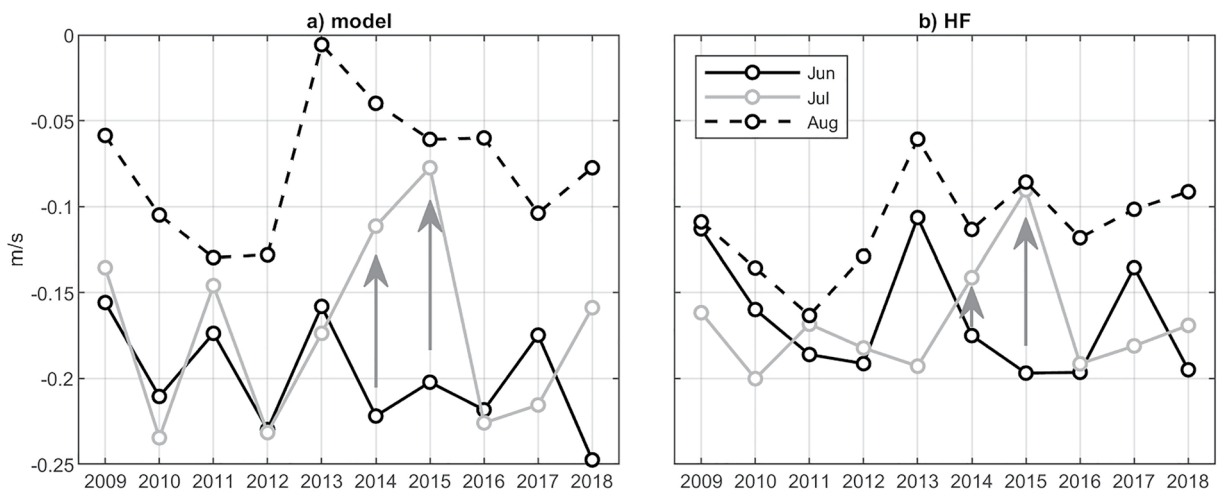

Figure 16. Monthly averaged alongshore surface current over the Oregon shelf as a function of the year for each summer month (June, July, and August). The values are obtained by time-averaging the daily values shown in Figure 6: (a) model, (b) HF radar. Arrows emphasize the early transition to anomalously low currents from June to July.

In future studies, it would be interesting to scrutinize the realistic model simulation presented here in relation to classical analytical and semi-analytical solutions for the CTW, in particular, to those studies that focused on relatively longer-period waves. Clarke and Van Gorder (1994) extended the theory to CTW with the periods as long as 2–5 years as related to the El Niño cycle. The phase speeds for the waves at those periods are estimated as 0.5–0.9 m s^{-1}, much lower than the speed of 2.5 m s^{-1} evident in the relatively short-period propagating alongshore anomalies in Figures 11b and 11c. In the present paper, we did not attempt to analyze the CTW in the spectral space and did not immediately see in the (y, t) diagrams wave patterns propagating at the lower speeds predicted by Clarke and Van Gorder (1994).

In addition to helping us answer some questions about the regional ocean variability, this study serves as a testament to the maturity of today's ocean models such as ROMS, providing an accurate description of the ocean dynamics on a wide spectrum of temporal and spatial scales. The model described here is planned to be included as the dynamical base of the new version of the West Coast Ocean Forecast System (WCOFS) currently operated by NOAA. The suite of model-data comparisons presented here provides a benchmark for future improvements to WCOFS as well as to any efforts modeling ocean dynamics in this area.

Data Availability Statement

The data used in this manuscript are available here: OSTIA SST (Donlon et al., 2012), https://podaac.jpl.nasa.gov/dataset/UKMO-L4HRfnd-GLOB-OSTIA, NDBC buoy surface temperature (https://www.ndbc.noaa.gov/), HF radar surface currents (https://cordc.ucsd.edu/), tide gauge sea level (https://tidesandcurrents.noaa.gov/), NH10 ADCP currents (https://ooinet.oceanobservatories.org), CTD T and S profiles at NH line (Risien et al., 2022), as well as CUGN glider T and S profiles (Rudnick, 2016) (https://spraydata.ucsd.edu/projects/CUGN/). Model outputs and the entire model setup are freely available upon request to anybody interested in future analyses or developments. NSF Ocean Observatories Initiative ADCP (CE02SHBP-LJ01D-05-ADCPTB104) data are available at https://ooinet.oceanobservatories.org.

Acknowledgments
The authors wish to thank Drs. K. Brink, P. MacCready, I. Rivin, and J. Pringle for useful discussions. The authors are grateful to Jennifer Fisher for providing the CTD profile data. Support for Risien and Cervantes was provided by NOAA's Climate Program Office, Climate Monitoring Program Grant NA17OAR4310154 and NASA Ocean Vector Winds Science Team Grant 80NSSC18K1611. Support by NASA Ocean Salinity Science Team Grant 80NSSC22K1003 is also acknowledged.

References

Allen, J. S., & Denbo, D. W. (1984). Statistical characteristics of the large-scale response of coastal sea level to atmospheric forcing. *Journal of Physical Oceanography*, *14*(6), 1079–1094. https://doi.org/10.1175/1520-0485(1984)014<1079:scotls>2.0.co;2

Amaya, D. J., Bond, N. E., Miller, A. J., & DeFlorio, M. J. (2016). The evolution and known atmospheric forcing mechanisms behind the 2013-2015 North Pacific warm anomalies. *US CLIVAR Variations*, *14*, 1–6.

Amaya, D. J., Jacox, M. G., Dias, J., Alexander, M. A., Karnauskas, K. B., Scott, J. D., & Gehne, M. (2022). Subseasonal-to-seasonal forecast skill in the California Current System and its connection to coastal Kelvin waves. *Journal of Geophysical Research: Oceans*, *127*, e2021JC017892. https://doi.org/10.1029/2021JC017892

Aoki, K., Kubokawa, A., Hideharu, S., & Yoshikazu, S. (2009). Midlatitude baroclinic Rossby waves in a high-resolution OGCM simulation. *Journal of Physical Oceanography*, *39*(9), 2264–2279. https://doi.org/10.1175/2009JPO4137.1

Battisti, D. S., & Hickey, B. M. (1984). Application of remote wind-forcing coastal trapped wave theory to the Oregon and Washington coasts. *Journal of Physical Oceanography*, *14*(5), 887–903. https://doi.org/10.1175/1520-0485(1984)014<0887:aorwfc>2.0.co;2;2

Bond, N. A., Cronin, M. F., Freeland, H., & Mantua, N. (2015). Causes and impacts of the 2014 warm anomaly in the NE Pacific. *Geophysical Research Letters*, *42*, 3414–3420. https://doi.org/10.1002/2015gl063306

Brink, K. H. (1991). Coastal-trapped waves and wind-driven currents over the continental shelf. *Annual Review of Fluid Mechanics*, *23*, 389–412. https://doi.org/10.1146/annurev.fl.23.010191.002133

Brink, K. H. (2006). Coastal-trapped waves with finite bottom friction. *Dynamics of Atmospheres and Oceans*, *41*, 172–190. https://doi.org/10.1016/j.dynatmoce.2006.05.001

Cavole, L. M., Demko, A. M., Diner, R. E., Giddings, A., Koester, I., Pagniello, C. M. L. S., et al. (2016). Biological impacts of the 2013–2015 warm-water anomaly in the northeast Pacific: Winners, losers, and the future. *Oceanography*, *29*, 273–285. https://doi.org/10.5670/oceanog.2016.32

Chao, Y., Farrara, J. D., Bjorkstedt, E. B., Chai, F., Chavez, F., Rudnick, D. L., et al. (2017). The origins of the anomalous warming in the California coastal ocean and San Francisco Bay during 2014–2016. *Journal of Geophysical Research: Oceans*, *122*, 7537–7557. https://doi.org/10.1002/2017JC013120

Chavez, F., & Messié, M. (2009). A comparison of eastern boundary upwelling ecosystems. *Progress in Oceanography*, *83*, 80–96. https://doi.org/10.1016/j.pocean.2009.07.032

Chen, Z., Shi, J., Liu, Q., Chen, H., & Li, C. (2021). A persistent and intense marine heatwave in the Northeast Pacific during 2019–2020. *Geophysical Research Letters*, *48*, e2021GL093239. https://doi.org/10.1029/2021GL093239

Clarke, A. J., & Van Gorder, S. (1994). On enso coastal currents and sea levels. *Journal of Physical Oceanography*, *24*, 661–680. https://doi.org/10.1175/1520-0485(1994)024<0661:oeccas>2.0.co;2

Connolly, T. P., Hickey, B. M., Shulman, I., & Thomson, R. E. (2014). Coastal trapped waves, alongshore pressure gradients, and the California undercurrent. *Journal of Physical Oceanography*, *44*, 319–342. https://doi.org/10.1175/JPO-D-13-095.1

Cummings, J. A., & Smedstad, O. M. (2013). Variational data analysis for the global ocean. In S. K. Park, & L. Xu (Eds.), *Data assimilation for atmospheric, oceanic and hydrologic applications*. (Vol. II, pp. 303–343). Springer-Verlag. https://doi.org/10.1007/978-3-642-35088-7_13

Davis, R. E., & Bogden, P. S. (1989). Variability on the California shelf forced by local and remote winds during the Coastal Ocean Dynamics Experiment. *Journal of Geophysical Research*, *94*(C4), 4763–4783. https://doi.org/10.1029/JC094IC04P04763

Di Lorenzo, E., & Mantua, N. (2016). Multi-year persistence of the 2014/15 North Pacific marine heatwave. *Nature Climate Change*, *6*, 1042–1048. https://doi.org/10.1038/nclimate3082

Donlon, C. J., Martin, M., Stark, J., Roberts-Jones, J., Fiedler, E., & Wimmer, W. (2012). The operational sea surface temperature and sea ice analysis (ostia) system. *Remote Sensing of Environment*, *116*, 140–158. https://doi.org/10.1016/j.rse.2010.10.017

Durski, S. M., Kurapov, A. L., Allen, J. S., Kosro, P. M., Egbert, G. D., Shearman, R. K., & Barth, J. A. (2015). Coastal ocean variability in the US Pacific northwest region: Seasonal patterns, winter circulation, and the influence of the 2009–2010 El Niño. *Ocean Dynamics*, *65*, 1643–1663. https://doi.org/10.1007/s10236-015-0891-1

Fairall, C. W., Bradley, E. F., Hare, J. E., Grachev, A. A., & Edson, J. B. (2003). Bulk parameterization of air-sea fluxes: Updates and verification for the COASRE algorithm. *Journal of Climate*, *16*, 571–591. https://doi.org/10.1175/1520-0442(2003)016<0571:bpoasf>2.0.co;2

Fisher, J. L., Peterson, W. T., & Rykaczewski, R. R. (2015). The impact of El Niño events on the pelagic food chain in the northern California Current. *Global Change Biology*, *21*, 4401–4414. https://doi.org/10.1111/gcb.13054

Frischknecht, M., Münnich, M., & Gruber, N. (2015). Remote versus local influence of ENSO on the California Current System. *Journal of Geophysical Research: Oceans*, *120*, 1353–1374. https://doi.org/10.1002/2014JC010531

Galperin, L. B., Kantha, L. H., Hassid, S., & Rosati, A. (1988). A quasi-equilibrium turbulent energy model for geophysical flows. *Journal of the Atmospheric Sciences*, *45*, 55–62. https://doi.org/10.1175/1520-0469(1988)045<0055:aqetem>2.0.co;2

Gan, J., & Allen, J. S. (2005). On open boundary conditions for a limited-area coastal model off Oregon. Part 1: Response to idealized wind forcing. *Ocean Modelling*, *8*(1–2), 115–133. https://doi.org/10.1016/j.ocemod.2003.12.006

Giddings, S. N., & MacCready, P. (2017). Reverse estuarine circulation due to local and remote wind forcing, enhanced by the presence of along-coast estuaries. *Journal of Geophysical Research: Oceans*, *122*, 10184–10205. https://doi.org/10.1002/2016JC012479

Gómez-Valdivia, F., Parés-Sierra, A., & Laura Flores-Morales, A. (2017). Semiannual variability of the California Undercurrent along the Southern California Current System: A tropical generated phenomenon. *Journal of Geophysical Research: Oceans*, *122*, 1574–1589. https://doi.org/10.1002/2016JC012350

Halliwell, G. R., & Allen, J. S. (1987). Wave-number frequency domain properties of coastal sea level response to alongshore wind stress along the west coast of North America. *Journal of Geophysical Research: Atmospheres*, *921*(11), 11761–11788. https://doi.org/10.1029/JC092iC11p11761

Illig, S., Cadier, E., Bachèlery, M.-L., & Kersalè, M. (2018). Subseasonal coastal-trapped wave propagations in the southeastern Pacific and Atlantic oceans: 1. A new approach to estimate wave amplitude. *Journal of Geophysical Research: Atmospheres*, *123*, 3915–3941. https://doi.org/10.1029/2017JC013539

Jacox, M. G., Desiree, T., Alexander, M. A., Hervieux, G., & Stock, C. A. (2019). Predicting the evolution of the 2014–2016 California Current System marine heatwave from an ensemble of coupled global climate forecasts. *Frontiers in Marine Science*, *6*, 497. https://doi.org/10.3389/fmars.2019.00497

Jacox, M. G., Hanzen, E. L., Zaba, K. D., Rudnick, D. L., Edwards, C. A., Moore, A. M., & Bograd, S. J. (2016). Impacts of the 2015–2016 El Niño on the California Current System: Early assessment and comparison to past events. *Geophysical Research Letters*, *43*, 7072–7080. https://doi.org/10.1002/2016GL069716

Junker, T., Mohrholz, V., Schmidt, M., Siegfried, L., & van der Plas, A. (2019). Coastal trapped wave propagation along the southwest African shelf as revealed by moored observations. *Journal of Physical Oceanography*, *49*(3), 851–866. https://doi.org/10.1175/JPO-D-18-0046.1

Kantha, L. H., & Clayson, C. A. (1994). An improved mixed layer model for geophysical applications. *Journal of Geophysical Research*, *99*(C12), 25235–25266. https://doi.org/10.1029/94jc02257

Kosro, P. M. (2005). On the spatial structure of coastal circulation off newport, Oregon, during spring and summer 2001 in a region of varying shelf width. *Journal of Geophysical Research*, *110*(C10), C1S06. https://doi.org/10.1029/2004JC002769

Kosro, P. M., Barth, J. A., & Strub, P. T. (1997). The coastal jet: Observations of surface currents over the Oregon continental shelf from HF radar. *Oceanography*, *10*(2), 53–56. https://www.jstor.org/stable/43924795

Kurapov, A. L., Allen, J. S., Egbert, G. D., Miller, R. N., Kosro, P. M., Levine, M., & Boyd, T. (2005). Distant effect of assimilation of moored currents into a model of coastal wind-driven circulation off Oregon. *Journal of Geophysical Research*, *110*, C02022. https://doi.org/10.1029/2003JC002195

Kurapov, A. L., Allen, J. S., Miller, R. N., & Egbert, G. D. (1999). Generalized inverse for baroclinic coastal flows. *Paper presented at the Third Conference on Coastal Atmospheric and Oceanic Prediction and Processes*, (Vol. *3–5*, pp. 101–106).

Kurapov, A. L., Egbert, G. D., Miller, R. N., & Allen, J. S. (2002). Data assimilation in a baroclinic coastal ocean model: Ensemble statistics and comparison of methods. *Monthly Weather Review*, *130*(4), 1009–1025. https://doi.org/10.1175/1520-0493(2002)130<1009:daiabc>2.0.co;2

Kurapov, A. L., Erofeeva, S. Y., & Myers, E. (2017). Coastal sea level variability in the US West Coast Ocean Forecast System (WCOFS). *Ocean Dynamics*, *67*, 23–36. https://doi.org/10.1007/s10236-016-1013-4

Kurapov, A. L., Rudnik, D. L., & Pelland, N. A. (2017). Seasonal and interannual variability in along-slope oceanic properties off the US West Coast: Inferences from a high-resolution regional model. *Journal of Geophysical Research: Oceans*, *122*, 5237–5259. https://doi.org/10.1002/2017JC012721

Marchesiello, P., McWilliams, J. C., & A, S. (2001). Ocean boundary conditions for long-term integration of regional ocean models. *Ocean Modelling*, *3*, 1–20. https://doi.org/10.1016/S1463-5003(00)00013-5

McCabe, R. M., Hickey, B. M., Kudela, R. M., Lefebvre, K. A., Adams, N. G., McCabe, R. M., et al. (2016). An unprecedented coastwide toxic algal bloom linked to anomalous ocean conditions. *Geophysical Research Letters*, *43*, 10366–10376. https://doi.org/10.1002/2016GL070023

McPhaden, M. J. (2015). Playing hide and seek with El Niño. *Nature Climate Change*, *5*, 791–795. https://doi.org/10.1038/nclimate2775

Mellor, G. L., & Yamada, T. (1982). Development of a turbulence closure model for geophysical fluid problems. *Reviews of Geophysics*, *20*(4), 851–875. https://doi.org/10.1029/RG020i004p00851

Molemaker, M. J., McWilliams, J. C., & Dewar, W. K. (2015). Submesoscale instability and generation of mesoscale anticyclones near a separation of the California undercurrent. *Journal of Physical Oceanography*, *45*(3), 613–629. https://doi.org/10.1175/JPO-D-13-0225.1

Musgrave, R. C. (2019). Energy fluxes in coastal trapped waves. *Journal of Physical Oceanography*, *49*(12), 3061–3068. https://doi.org/10.1175/JPO-D-18-0172.1

Myers, T. A., Mechoso, C. R., Cesana, G. V., DeFlorio, M. J., & Waliser, D. E. (2018). Cloud feedback key to marine heatwave off Baja California. *Geophysical Research Letters*, *45*, 4345–4352. https://doi.org/10.1029/2018GL078242

Oke, P. R., Allen, J. S., Miller, R. N., Egbert, G. D., & Kosro, P. M. (2002). Assimilation of surface velocity data into a primitive equation coastal ocean model. *Journal of Geophysical Research*, *107*(C9), 3122. https://doi.org/10.1029/2000jc000511

Pelland, N. A., Eriksen, C. C., & Lee, C. M. (2013). Subthermocline eddies over the Washington continental slope as observed by seagliders, 2003–09. *Journal of Physical Oceanography*, *43*(10), 2025–2053. https://doi.org/10.1175/JPO-D-12-086.1

Peterson, W. T., Fisher, J. L., Strub, P. T., Du, X., Risien, C., Peterson, J., & Shaw, C. T. (2017). The pelagic ecosystem in the Northern California Current off Oregon during the 2014–2016 warm anomalies within the context of the past 20 years. *Journal of Geophysical Research: Oceans*, *122*, 7267–7290. https://doi.org/10.1002/2017JC012952

Piatt, J. F., Parrish, J. K., Renner, H. M., Schoen, S. K., Jones, T. T., Arimitsu, M. L., et al. (2020). Extreme mortality and reproductive failure of common murres resulting from the northeast Pacific marine heatwave of 2014-2016. *PLoS One*, *15*(1), e0226087. https://doi.org/10.1371/journal.pone.0226087

Pierce, S. D., Smith, R. L., Kosro, P. M., Barth, J. A., & Wilson, C. D. (2000). Continuity of the poleward undercurrent along the eastern boundary of the mid-latitude north Pacific. *Deep-Sea Research Part II*, *47*(5–6), 811–829. https://doi.org/10.1016/S0967-0645(99)00128-9

Risien, C. M., Fewings, M. R., Fisher, J. L., Peterson, J. O., & Morgan, C. A. (2022). Spatially gridded cross-shelf hydrographic sections and monthly climatologies from shipboard survey data collected along the Newport Hydrographic Line, 1997–2021. [Dataset]. Data in Brief, *41*, 107922. https://doi.org/10.1016/j.dib.2022.107922

Rudnick, D. L., Owens, W. B., Johnston, T. M. S., Karnauskas, K. B., Jakoboski, J., & Todd, R. E. (2021). The equatorial current system west of the Galápagos Islands during the 2014–16 El Niño as observed by underwater gliders. *Journal of Physical Oceanography*, *51*, 3–17. https://doi.org/10.1175/JPO-D-20-0064.1

Rudnick, D. L., Zaba, K. D., Todd, R. E., & Davis, R. E. (2017). A climatology of the California Current System from a network of underwater gliders. *Progress in Oceanography*, *154*, 64–106. https://doi.org/10.1016/j.pocean.2017.03.002

Samelson, R. M. (2017). Time-dependent linear theory for the generation of poleward undercurrents on eastern boundaries. *Journal of Physical Oceanography*, *47*(12), 3037–3059. https://doi.org/10.1175/JPO-D-17-0077.1

Samelson, R. M., Barbour, P., Barth, J., Bielli, S., Boyd, T., Chelton, D., et al. (2002). Wind stress forcing of the Oregon coastal ocean during the 1999 upwelling season. *Journal of Geophysical Research*, *107*(C5), 2-1–2-8. https://doi.org/10.1029/2001JC000900

Schwing, F. B., Murphree, T., de Witt, L., & Green, P. M. (2002). The evolution of oceanic and atmospheric anomalies in the northeast Pacific during the El Niño and La Niña events of 1995–2001. *Progress in Oceanography*, *54*, 459–491. https://doi.org/10.1016/s0079-6611(02)00064-2

Shchepetkin, A. F., & McWilliams, J. C. (2003). A method for computing horizontal pressure-gradient force in an oceanic model with a nonaligned vertical coordinate. *Journal of Geophysical Research*, *108*(C3), 3090. https://doi.org/10.1029/2001JC001047

Shchepetkin, A. F., & McWilliams, J. C. (2005). The regional oceanic modeling system (ROMS): A split-explicit, free-surface, topography-following-coordinate oceanic model. *Ocean Modelling*, 9, 347–404. https://doi.org/10.1016/j.ocemod.2004.08.002

Springer, S. R., Samelson, R. M., Allen, J. S., Egbert, G. D., Kurapov, A. L., Miller, R. N., & Kindle, J. C. (2009). A nested grid model of the Oregon coastal transition zone: Simulations and comparisons with observations during the 2001 upwelling season. *Journal of Geophysical Research*, *114*, C02010. https://doi.org/10.1029/2008jc004863

Suryan, R. M., Arimitsu, M. L., Coletti, H. A., Hopcroft, R. R., Lindeberg, M. R., Barbeaux, S. J., et al. (2021). Ecosystem response persists after a prolonged marine heatwave. *Scientific Reports*, *11*, 6237. https://doi.org/10.1038/s41598-021-83818-5

Wang, D.-P., & Mooers, C. N. K. (1976). Coastal-trapped waves in a continuously stratified ocean. *Journal of Physical Oceanography*, *6*(6), 853–863. https://doi.org/10.1175/1520-0485(1976)006<0853:ctwiac>2.0.co;2

Zaba, K. D., & Rudnick, D. L. (2016). The 2014–2015 warming anomaly in the southern California Current System observed by underwater gliders. *Geophysical Research Letters*, *43*, 1241–1248. https://doi.org/10.1002/2015GL067550

Zaba, K. D., Rudnick, D. L., Cornuelle, B. D., Gopalakrishnan, G., & Mazloff, M. R. (2020). Volume and heat budgets in the coastal California Current System: Means, annual cycles, and interannual anomalies of 2014–16. *Journal of Physical Oceanography*, *50*, 1435–1436. https://doi.org/10.1175/JPO-D-19-0271.1